공학박사 학위논문

Rheology and microstructure of non-Brownian suspensions under shear flow investigated by the lattice Boltzmann method

Lattice Boltzmann 수치모사 기법을 이용한

전단유동 하에서의 **non-Brownian** 현탁액의

유변물성 및 미세구조 연구

2015년 2월

서울대학교 대학원

화학생물공학부

이 영 기

Rheology and microstructure of non-Brownian suspensions under shear flow investigated by the lattice Boltzmann method

지도교수 이 승 종

이 논문을 공학박사 학위논문으로 제출함
2015년 2월

서울대학교 대학원
화학생물공학부
이 영 기

이영기의 공학박사 학위논문을 인준함
2015년 2월

위 원 장 _____ (인)

부위원장 _____ (인)

위 원 _____ (인)

위 원 _____ (인)

위 원 _____ (인)

Abstract

Rheology and microstructure of non-Brownian suspensions under shear flow investigated by the lattice Boltzmann method

Young Ki Lee
School of Chemical and Biological Engineering
The Graduate School
Seoul National University

Particle suspensions are used extensively in many industrial applications such as manufacturing of batteries, electronic components, solar cells, printed electronics, and so on. The rheological properties of the suspensions are changed during the process, which affects the quality of the final products. Therefore, understanding their rheology is essential to manufacturing. It is strongly correlated with its microstructue, and numerical simulation is highly desirable to explore their relations. In this study, we investigated the rheology and microstructure of non-Brownian suspensions in both steady and oscillatory shear flow. To describe the suspension system, the Lattice Boltzmann method (LBM) coupled with the smoothed profile method (SPM) was adopted.

First, the rheology of non-Brownian suspensions under steady shear flow was studied. The effect of particle volume fraction and particle Reynolds number on the rheology of the suspension was investigated, and the correlation of local quantities

such as local shear stress and local particle volume fraction was analyzed. Previous studies focused only on the bulk rheology of complex fluids because the local rheology was not accessible due to the technical limitations. On the other hand, we adopted the novel algorithm, called the method of planes (MOP) to correlate non-Newtonian fluid behavior with the structural evolution of concentrated suspensions. At low particle Reynolds number, an increase in the relative shear viscosity was observed with an increase in the particle volume fraction, and the results corresponded well with the Krieger-Dougherty equation. Shear thickening was successfully captured with highly concentrated suspensions at high particle Reynolds number. By analyzing the microstructure, we observed that large clusters were formed at high particle Reynolds number, and they were aligned to the compressive axis with shear thickening. Both the local rheology and the local structure of the suspensions were analyzed, and we found that the linear correlation between the local particle stress and local particle volume fraction was dramatically reduced during shear thickening. These results prove that the local structure of the suspensions affect both local and bulk rheology during shear thickening.

Secondly, nonlinear rheological responses of concentrated hard-sphere suspensions under oscillatory shear flow were investigated. It is known that the concentrated suspensions show a peculiar nonlinear behavior under large amplitude oscillatory shear (LAOS) flow, so-called strain stiffening, in which the complex viscosity or dynamic moduli begin to increase at critical strain amplitude. Although this phenomenon has been widely observed in experiments, its mechanism has never been explored in a systematic way. To clarify this mechanism, numerical simulation was performed by LBM coupled with SPM. Dynamic moduli of the suspensions were investigated for varying strain amplitudes at a fixed angular

frequency, and the strain stiffening was clearly observed at high strain amplitudes. With strain stiffening, the shear stress began to show distorted waveform near the critical strain amplitude, and this behavior was quantified by the Fourier transform (FT) and the stress decomposition. Microstructure of the suspensions was also investigated to find the origin of strain stiffening. The bond order parameter was applied to quantify the structural change of the suspensions, and it was found that the distortion in shear stress and the increase of dynamic moduli are strongly correlated with the ordering of particles during the oscillatory shear flow. Our results clearly demonstrate how the ordering of particles affects nonlinear rheological behavior of non-Brownian suspensions in large amplitude oscillatory shear flow.

Keywords: Rheology, microstructure, non-Brownian suspensions, hard-sphere, shear thickening, strain stiffening, lattice Boltzmann method, smoothed profile method, method of planes

Student Number: 2008-21101

Contents

List of Figures

List of Tables

Chapter 1. Introduction

1.1. Background of suspension rheology

Concentrated particle suspensions are widely used in industry, and its various rheological behaviors are important in designing the materials and processes [1]. One of the issues in suspension rheology is the shear thickening which is often observed in concentrated suspensions. The shear thickening is a rheological behavior in which the apparent viscosity increases with shear rate, and it has been widely observed for suspensions of hard-spheres and electrostatically stabilized dispersions [2-9].

Many studies have been performed to understand the mechanism of shear thickening in steady shear flow. Structural evolution of particle suspensions during shear thickening was probed by rheo-optical experiments [7-9]. However, despite the progress of experimental techniques, direct observation of the microstructure still has many limitations. Therefore, numerical simulation needs to be done to support experimental observations and to theoretically explain the various phenomena of these complex fluids [10-20]. Brady and co-workers analyzed the nonequilibrium behavior of Brownian (colloidal) suspension by the Stokesian dynamics (SD) [10-12] and accelerated Stokesian dynamics (ASD) simulation techniques [13]. Foss and Brady [12] investigated the non-equilibrium behavior of concentrated Brownian suspensions under a simple shear flow. They focused on the effect of the Peclet number on the particle dynamics, and shear thickening at the high Peclet number region (hydrodynamic dominant region) was successfully captured. In that study, they showed that the lubrication force has a crucial role in

forming clusters among the approaching particles, and these clusters can trigger shear thickening in hard-sphere suspensions. They also explained how anisotropy in the pair-distribution function affects the rheology of the suspensions. In this way, the SD algorithm contributed to understanding suspension rheology including shear thickening, but it also has several limitations. One is that only the flow behavior can be explained at low Reynolds number, that is to say, only a system in which the inertia effect is negligible can be considered. In real processes, suspensions that include various sizes of particles from several nanometers to several millimeters are commonly used. Furthermore, they are usually transported under complex flow situations at a high flow rate. In these conditions, the inertia may not be negligible. Therefore, understanding flow behavior with inertia is quite important. Taking inertia into consideration at finite Reynolds number is still challenging. Though a study on particle suspensions with inertia has been carried out by direct numerical simulation (DNS) [14], only a few studies have been done due to high computational cost.

Recently, the lattice Boltzmann method (LBM) has been introduced, and it has been widely applied to investigate various fluid dynamics problems as well as the dynamics of particle suspensions [15,16] at finite Reynolds number. Shakib-Manesh *et al*. [17] successfully predicted the relative shear viscosity of non-Brownian suspensions in a two-dimensional (2D) Couette flow by LBM, and they reported on the shear thickening behavior of hard-sphere suspensions at high particle Reynolds number. Raiskinmäki *et al*. [18] captured shear thickening, and they carefully explored the correlate shear thickening with particle clustering in a regime where hydrodynamic forces are dominant. Kromkamp *et al*. [19] also studied non-Brownian suspensions by LBM, and they compared the flow behaviors

of 2D and 3D suspensions in a laminar flow. They investigated the shear viscosity of the suspensions and reasonable results were confirmed in both cases. Kulkarni and Morris [20] studied the rheology of 3D particle suspensions at finite Reynolds number. Increment of the normal stress difference was observed, and anisotropy in microstructure at finite Reynolds numbers was also quantified through the pair distribution function.

Even though a significant number of experimental and simulation studies have been performed to understand shear thickening in steady shear flow (steady shear thickening), only limited works have addressed rheological behaviors of concentrated suspensions for the transient response in oscillatory shear flow [21-26]. In the oscillatory shear test, shear thickening behavior has also been reported (dynamic shear thickening). Laun *et al*. [21] investigated strain hardening of a polymer latex dispersion under the oscillatory shear flow, and they observed the increase of complex viscosity with the increase in strain amplitude at a fixed angular frequency. They also explored the effect of angular frequency on the critical strain amplitude. Dynamic shear thickening was decreased as the angular frequency increased, and it eventually reached to a plateau at higher frequencies. Boersma *et al.* [22] reported dynamic shear thickening of mono dispersed silica suspensions. In their work, critical shear rate was well interpreted in terms of the steady-state shear response (i.e., $\dot{\gamma}_c^{dynamic} = \gamma_{0,c}\omega \simeq \dot{\gamma}_c^{steady}$) at a low angular frequency, but difference was observed at higher angular frequencies. The frequency dependence on the critical shear rate was also observed in other experiments [23-26], which is most distinguishing characteristic of dynamic shear thickening compared to steady shear thickening. Therefore, shear thickening in dynamic shear flow has been regarded as a different phenomenon with steady shear thickening, and this is called as "dynamic

shear thickening" or "strain stiffening" [26,27]. Recently, Nam *et al*. [27] investigated nonlinear behavior of non-Brownian suspensions near liquid and crystal coexistence region. Experiments were performed for varying conditions, and strain stiffening was observed at high strain amplitude regions. With strain stiffening, the shear stress started to distort near the critical strain amplitude, and this nonlinear response was quantitatively analyzed. Strain stiffening has also been reported in other studies [23,25], but the origin of strain stiffening was scarcely discussed. Although, the formation of hydrocluster and the rearrangement of particles under dynamics shear flow were hypothesized as the key mechanism of strain stiffening, it was not clearly proved yet.

1.2. Objective

Our goal is to clarify the mechanism of various rheological behavior of non-Brownian suspensions under steady and oscillatory shear flow. To achieve it, rheological properties and microstructures of suspension were investigated by the lattice Boltzmann method (LBM) coupled with the smoothed profile method (SPM) [28].

First, rheology of non-Brownian suspension under steady shear flow was investigated. The effects of the particle volume fraction and the particle Reynolds number on rheology of suspension were explored, and the correlation of local quantities such as local shear stress and local particle volume fraction were also analyzed. Although there have been many studies on the non-Newtonian behavior of suspensions, only wall shear stress or bulk shear stress [29] has been measured in simulations. They have limitations in investigating local shear stress, and it is hard to explain how local structural evolution affects the rheology in a local region and subsequently, the bulk rheology of suspensions. On the other hand, we adopted the novel algorithm, called method of planes (MOP) [30] to correlated non-Newtonian fluid behavior with the structural evolution of concentrated suspensions.

Secondly, the rheology of concentrated hard-sphere suspensions in the liquid and crystal coexistence region was investigated by the lattice Boltzmann method (LBM). In contrast to previous simulation studies using LBM that were mostly focused on the suspension rheology in steady shear flow [17-20], the rheological properties of the suspensions under the oscillatory shear flow were investigated to find the origin of strain stiffening. This simulation was designed based on Nam *et al.*'s experiments [27], and the microstructures and rheological behaviors were

carefully investigated for non-Brownian suspensions in the liquid and crystal coexistence region. As far as we are concerned, no one has yet observed strain stiffening behavior of the suspensions by numerical simulation, and there was no report which directly correlated rheology and microstructures in the liquid and crystal coexistence region. Therefore, the present work provides an inspiration to understanding the nonlinear rheology of concentrated suspensions under dynamic oscillatory shear flow.

1.3. Outline of the thesis

In chapter 2, numerical methods are introduced. Theories of lattice Boltzmann method (LBM) and smoothed profile method (SPM) are reviewed in chapter 2.1 and chapter 2.2. Boundary conditions are briefly described in chapter 2.3. The conception of method of plane (MOP) is explained in chapter 2.4, and extensive validation of the present algorithm is presented in chapter 2.5. In chapter 3, results of numerical simulation for non-Brownian suspensions are provided. The rheological behaviors of suspensions in steady shear flow are discussed in Section 3.1. The effects of the particle volume fraction and the particle Reynolds number on the rheology and the microstructure of suspension are examined. In addition, correlations between local quantities such as local shear stress and local particle volume fraction are also explored. The strain stiffening phenomenon of hard-sphere suspensions in liquid and crystal coexistence region is discussed in chapter 3.2. Nonlinear rheological responses and microstructures of suspensions under large strain oscillatory shear (LAOS) flow are explored by numerical simulation, and the key mechanism of strain stiffening is suggested. Finally, conclusions are given in chapter 4.

Chapter 2. Numerical method

2.1. Lattice Boltzmann method (LBM)

Since its introduction two decades ago, the lattice Boltzmann method (LBM) has been recognized as a useful tool in computational fluid dynamics, and it has been widely adopted for various applications such as microfluidics, turbulent flows and multiphase systems due to its easy implementation [15].

In LBM, macroscopic dynamics can be described by the lattice Boltzmann equation (LBE) which is an approximate and discretized form of the Boltzmann equation. While conventional methods such as the finite element method (FEM) or finite volume method (FVM) directly solve Navier–Stokes (NS) equations, the LBM introduces virtual particles which are the packets of mesoscopic particles [15,16]. The evolution of the probability distribution function is given by the lattice-Boltzmann equation with the Bhatnagar–Gross–Krook (BGK) collision operator [31] which takes the form of Eq. (1). By solving this equation, the incompressible Navier-Stokes (NS) equations can be correctly recovered [31].

$$f_i(\mathbf{x}+\mathbf{c}_i\Delta t, t+\Delta t) - f_i(\mathbf{x},t) = -\frac{1}{\tau}\left[f_i(\mathbf{x},t) - f_i^{eq}(\mathbf{x},t)\right]. \tag{1}$$

The LBM algorithm consists of streaming and collision steps. At the streaming step, the probability distribution function from the previous time step is propagated along the discretized velocity vector $\mathbf{c}_i$ to the next neighbor lattice nodes. This process can be imposed by the left-hand side of Eq. (1), where $\mathbf{x}$ is the position of the lattice

node at time t; $\mathbf{c}$ is the discrete velocity, and f_i is the distribution function for the i direction. τ denotes the dimensionless relaxation time of the solvent, and it is related to the kinematic viscosity, $\nu = c_s^2(\tau - 1/2)\Delta x^2 / \Delta t$ [31].

In our study, the D2Q9 lattice model was used which was designed to consider nine direction velocities in two-dimensional space [15]. In this system, the speed of sound has the form of $c_s = \sqrt{1/3}\Delta x / \Delta t$, where Δx and Δt denote the lattice spacing and time step, respectively. After the streaming step, the probability distribution function is determined for each lattice point with the collision step, according to the right-hand side of Eq. (1). During this process, momentum conservation is constrained by the equilibrium distribution, f_i^{eq}, which is determined by Eq. (2).

$$f_i^{eq}(\mathbf{x}) = w_i \rho \left[1 + \frac{\mathbf{c}_i \cdot \mathbf{u}}{c_s^2} + \frac{(\mathbf{c}_i \cdot \mathbf{u})^2}{2c_s^4} - \frac{\mathbf{u} \cdot \mathbf{u}}{2c_s^2} \right]. \tag{2}$$

The equilibrium distribution can be obtained by the truncated form of the Maxwell distribution, and it is well known as a good approximation for small Mach numbers [31].

The macroscopic properties of the solvent such as the density ρ and the velocity $\mathbf{u}$ are obtained from the zeroth and first velocity moments of the distribution function f_i shown in Eq. (3) and Eq. (4).

$$\rho = \sum_i f_i, \tag{3}$$

$$\rho \mathbf{u} = \sum_i f_i \mathbf{c}_i. \tag{4}$$

Direction dependent weight coefficients w_i and the lattice velocity $\mathbf{c}_i$ were used according to Table. 1.

Table 1

Weight coefficients, w_i and the lattice velocity, $\mathbf{c}_i$ in D2Q9 lattice model.

	i=0	i=1	i=2	i=3	i=4	i=5	i=6	i=7	i=8
w_i	4/9	1/9	1/9	1/9	1/9	1/36	1/36	1/36	1/36
$\mathbf{c}_i$	(0,0)	(1,0)	(0,1)	(-1,0)	(0,-1)	(1,1)	(-1,1)	(-1,-1)	(1,-1)

2.2. Smoothed profile method (SPM)

Various algorithms have been suggested to consider the motion of solid particles in LBM [32-36]. They have been widely used to investigate the dynamics and rheology of particle suspensions [17-20].

In this study, the smoothed profile method (SPM) was adopted, which has been successfully combined with LBM [28] and widely applied to particle systems [37-39]. SPM is a promising numerical algorithm, which considers multi-body hydrodynamic interactions among solid particles accurately and efficiently, and has been successfully applied to a neutrally buoyant cylinder under simple shear flow, sedimentation of two circular cylinders and so on [28].

In SPM, the boundaries between solid objects and the host solvent are replaced with a continuous interface by assuming a smoothed profile so that the discontinuity problem, which arises on the boundary of solid objects, can be dramatically reduced. SPM is also efficient because it does not need additional Lagrangian nodes [37] near the surface of solid objects. Furthermore, it is more accurate for momentum conservation than that of other link-based methods [32-34]. In SPM, the profile function $\phi_P(\mathbf{x})$ that defines spherical particle (cylinder in 2D) can be chosen arbitrarily, but in this study, it was defined in the form of Eq. (5) as follows:

$$\phi_P(\mathbf{x}) = \frac{1}{2}\left[1 + \tanh\frac{R - |\mathbf{x} - \mathbf{X}|}{\xi}\right]. \tag{5}$$

Here, R is the radius of solid particle; $\mathbf{X}$ is the center position of the solid particle,

and **x** is the position of the lattice node. In the fluid region, $\phi_P = 0$ while $\phi_P = 1$ in the solid particle region, and its value changes continuously at the interfacial region. The interface thicknesses was controlled by parameter ξ, and the accuracy can be enhanced by controlling ξ [28,37]. In this study, $\xi = 1$ was applied which is commonly used in the literature, and the cutoff radius was set as $R_{\text{cutoff}} = R + \Delta x$ for an efficient calculation.

The solvent-solid interaction force on solid boundary node, **x** at time t, can be evaluated by Eq. (6) with the assumption that the forces and torque are distributed during the interval time Δt as follows:

$$\mathbf{f}_P(\mathbf{x},\mathrm{t}) = \phi_P(\mathbf{x},t)\left[\mathbf{u}_P(\mathbf{x},t) - \mathbf{u}(\mathbf{x},t)\right] / \Delta t, \tag{6}$$

where **u** is the macroscopic velocity at the solvent node which was defined in Eq. (4), and $\mathbf{u}_P$ is the velocity at solid node. $\mathbf{u}_P$ is defined in terms of the translation velocity of the solid particle **U** and the angular velocity of the solid particle $\boldsymbol{\Omega}$ at the lattice node **x** covered by solid particles.

$$\mathbf{u}_P(\mathbf{x},t) = \mathbf{U} + \boldsymbol{\Omega} \times (\mathbf{x} - \mathbf{X}). \tag{7}$$

The hydrodynamic force affected by the solid particles to the solvent boundary node is calculated by Eq. (8),

$$\mathbf{f}_H(\mathbf{x},t) = -\mathbf{f}_P(\mathbf{x},\mathrm{t}), \tag{8}$$

and then, the hydrodynamic force $\mathbf{f}_H$ is added to the collision operator in Eq. (1) as

a body force which considers the interaction between two phases. This process is presented by Eq. (9).

$$f_i(\mathbf{x}+\mathbf{c}_i\Delta t, t+\Delta t) - f_i(\mathbf{x},t) = -\frac{1}{\tau}\left[f_i(\mathbf{x},t) - f_i^{eq}(\mathbf{x},t)\right] + \frac{w_i \Delta t}{c_s^2}\left[\mathbf{f}_H(\mathbf{x},t)\cdot\mathbf{c}_i\right]. \tag{9}$$

The hydrodynamic force $\mathbf{F}_H$ and torque $\mathbf{T}_H$, which influence each particle, are calculated by Eq. (10) and (11), respectively.

$$\mathbf{F}_H = \sum_{\mathbf{x}\in V_p} \rho(\mathbf{x})\mathbf{f}_P(\mathbf{x},\mathrm{t}), \tag{10}$$

$$\mathbf{T}_H = \sum_{\mathbf{x}\in V_p} (\mathbf{x}-\mathbf{x}_s)\times\rho(\mathbf{x})\mathbf{f}_P(\mathbf{x},\mathrm{t}). \tag{11}$$

Translation velocity and angular velocity of the solid particles at a new time step are obtained by Eq. (12) and (13),

$$\mathbf{V}(t+\Delta t) = \mathbf{V}(t) + \frac{\mathbf{F}_H}{M_P}\Delta t, \tag{12}$$

$$\mathbf{\Omega}(t+\Delta t) = \mathbf{\Omega}(t) + \frac{\mathbf{T}_H}{I_P}\Delta t. \tag{13}$$

The mass of a solid particle M_P and the moment of inertia I_P are defined by Eq. (14) and (15), where ρ_P denotes the density of a solid particle.

$$M_P = \rho_P \pi R^2, \tag{14}$$

$$I_P = 0.5 M_P R^2. \tag{15}$$

The particle position is updated from the new particle velocity, which was obtained by Eq. (12), and it was integrated by the Adams–Bashforth method [40], as in Eq. (16) which has a second-order accuracy.

$$\mathbf{X}(t+\Delta t)=\mathbf{X}(t)+\left(\frac{3}{2}\mathbf{V}(t+\Delta t)-\frac{1}{2}\mathbf{V}(t)\right)\Delta t. \tag{16}$$

To prevent overlap among solid particles, the short range repulsive potential in Eq. (17) was additionally imposed. The potential has the form of the Weeks, Chandler and Andersen (WCA) which has been widely used to describe nearly hard-spheres [41]. σ is the diameter of a solid particle; r is the particle to particle center distance, and ε is the potential strength. In this work, ε was set to 0.1, and it was determined by trial and error not to allow overlap between the particles at the highest shear rate we could cover.

$$U_{PP}(r)=\begin{cases}\varepsilon\left[\left(\dfrac{\sigma}{r}\right)^{36}-\left(\dfrac{\sigma}{r}\right)^{18}\right], & r\le 2^{1/18}\sigma\\ 0, & r>2^{1/18}\sigma.\end{cases}, \tag{17}$$

When two particles come into close contact with each other, the lubrication force becomes important. However, the lubrication force cannot be exactly resolved with LBM when the gap distance between two particles is on the order of one lattice spacing due to the discretization of the particles and fluids. To overcome this problem, a lubrication correction method based on an explicit calculation of the lubrication force was introduced [19,33]. For a 3D system, it is given by,

$$\mathbf{F}_{\text{lub}} = \begin{cases} -6\pi\eta \dfrac{a_1^2 a_2^2}{(a_1+a_2)^2}\left(\dfrac{1}{h}-\dfrac{1}{h_c}\right)\mathbf{U}_{12}\cdot\hat{\mathbf{R}}_{12}, & h < h_c, \\ 0, & h > h_c. \end{cases} \tag{18}$$

Here, a_1 and a_2 denote the radius of two solid particles, and they have the same value a in the monodisperse system. η means the solvent viscosity; $\mathbf{U_{12}} = \mathbf{U_1} - \mathbf{U_2}$ denotes the relative velocity of the particles, and $\widehat{\mathbf{R}}_{12} = (\mathbf{R_1} - \mathbf{R_2})/|\mathbf{R_1} - \mathbf{R_2}|$ is a unit vector between two particles. h is the surface to surface distance of two particles and h_c is the cut-off distance.

In this study, the analytically derived equation by Kromkamp *et al*. [19] was adopted for a 2D particle (cylinder), which is defined as follows.

$$\mathbf{F}_{\text{lub}} = \begin{cases} -\dfrac{1}{2}\eta\mathbf{U}_{12}\cdot\hat{\mathbf{R}}_{12}\hat{\mathbf{R}}_{12}\left(\left(\dfrac{a_1+a_2}{h}\right)^{3/2}\left(F_0+\dfrac{h}{a_1+a_2}F_1\right)-\left(\dfrac{a_1+a_2}{h_c}\right)^{3/2}\left(F_0+\dfrac{h_c}{a_1+a_2}F_1\right)\right), & h < h_c, \\ 0, & h > h_c. \end{cases} \tag{19}$$

$h_c = 1.5\ \Delta x$ was adopted, and it was determined by the lubrication test for two approaching particles (it will be discussed in the next section). Even though this value is a little different from the optimum cut-off distance used by Kromkamp *et al*. [19] (1.1 Δx for 3D system and 2.0 Δx for 2D system), the verification test confirms that $h_c = 1.5\ \Delta x$ is also reasonable in this system. F_0 is the numerical constant, and F_1 is the first order correction to the lubrication limit, $h / 2a << 1$. In this study, they were determined as $\frac{3}{4}\pi\sqrt{2}$ and $\frac{231}{80}\pi\sqrt{2}$, respectively, from the analytical

derivation by Kromkamp *et al*. [19].

2.3. Boundary condition

To apply shear flow in a confined system, the halfway bounce-back method [32,33] was imposed which is commonly used to describe the no-slip or moving wall boundary condition in LBM. In this algorithm, fluid distribution hitting a solid wall during propagation is bounced back in the direction it came from, and this microscopic boundary rule finally leads to a no-slip behavior of the macroscopic fluids at the wall.

To describe the moving wall with velocity $\mathbf{u}_{\mathrm{w}}$, the original equation is modified as in Eq. (20), where f_i^* means the fluid distribution after the collision process, and i' denotes the inverse direction of i. The newly added term in the right-hand side of Eq. (20) captures the additional momentum transfer by the motion of the wall.

$$f_{i'}(\mathbf{x}, t+\Delta t) = f_i^*(\mathbf{x}, t) - \frac{2w_i \rho(\mathbf{x}, t)\mathbf{u}_{\mathrm{w}} \cdot \mathbf{c}_i}{c_s^2}. \tag{20}$$

During the bounce back process, the wall momentum exchange Δp can be derived by Eq. (21),

$$\Delta p_{i'}(\mathbf{x}_w, t+\frac{1}{2}\Delta t) = \left(2f_i^*(\mathbf{x}, t) - \frac{2w_i \rho(\mathbf{x}, t)\mathbf{u}_{\mathrm{w}} \cdot \mathbf{c}_i}{c_s^2} \right) \mathbf{c}_i. \tag{21}$$

It is straightforward to evaluate the wall shear stress through the wall momentum exchange Δp per time Δt. It can be obtained by Eq. (22), where A is the wall surface area (the length of the wall boundary in a 2D case)

$$\sigma^{w} = \frac{\Delta p_{i'}}{\Delta t A}. \tag{22}$$

2.4. Method of planes (MOP)

Measuring rheological properties from wall shear stress (WSS) is realistic and commonly accepted in rheometry. However, it does not allow the separation of solvent and particle contributions from the total stress, and the local shear stress of the fluid cannot be easily accessed. If the system is nonhomogeneous, it is more desirable to evaluate the local contribution of the solvent and particle to the total stress. However, it is hardly accessible in numerical simulations. To overcome this problem, a novel algorithm, the so-called method of planes (MOP), was proposed by Todd *et al.* [42]. This algorithm has successfully predicted the local stress of a simple liquid, and has been further applied to polymer melts [43]. Recently, it was extended to LBM coupled with the immersed boundary method (IBM) [30]. In this study, we applied the MOP algorithm to the smoothed profile method (SPM) with a slight modification. Even in this case, the solvent and particle contributions to total stress can be locally measured at each of the planes along the shear gradient direction in the same manner as the original algorithm [30].

The solvent shear stress in each lattice node **x** at time *t* can be obtained by Eq. (23) [44,45], and the local solvent stress at plane *Y* was defined as Eq. (24), where *j* means the lattice nodes in plane *Y*.

$$\sigma_{xy}^{s}(\mathbf{x},t) = (1-\frac{\tau}{2})\sum_{i}(f_i(\mathbf{x}) - f_i^{eq}(\mathbf{x}))c_{xi}c_{yi}, \tag{23}$$

$$\sigma_{xy,local}^{s}(Y,t) = \frac{1}{A}\sum_{j}\sigma_{xy}^{s}(j,t). \tag{24}$$

Imaginary plane y between lattice planes Y and $Y + \Delta Y$ (usually, ΔY = 1 in LBM) is assumed to calculate the local particle stress, and local particle stress at plane y is obtained by Eq. (25). In Krüger's work [30], F_{jx}(t) was defined as the x-component of the force imposed on the lattice node j at time t, and it could be directly measured by the interfacial tension or the membrane forces on the Lagrangian nodes (for soft particles). In the present SPM system, F_{jx} can be alternatively changed to the x-component of the hydrodynamic force $\mathbf{f}_H$ on a solid particle in Eq. (9), and is considered at the lattice nodes covered with solid particles. The sign function, sgn(x) has the values of +1 or -1 depending on the sign of x, and A denotes the length of the domain size in the x-direction (flow direction in our system) in the case of a 2D simulation. Local particle stress at lattice node Y can be obtained by the average of two planes separated by one lattice constant ΔY; it is given by Eq. (26). Finally, the total stress in plane Y can be locally evaluated by the sum of each stress component as shown in Eq. (27).

$$\sigma^{p}_{xy,local}(y,t) = \frac{1}{2A}\sum_{j} F_{jx}(t)\,\mathrm{sgn}(y - Y), \tag{25}$$

$$\sigma^{p}_{xy,local}(Y,t) = \frac{1}{2}\left(\sigma^{p}_{xy,local}(Y + \frac{\Delta Y}{2}, t) + \sigma^{p}_{xy,local}(Y - \frac{\Delta Y}{2}, t) \right), \tag{26}$$

$$\sigma^{tot}_{xy,local}(Y,t) = \sigma^{s}_{xy,local}(Y,t) + \sigma^{p}_{xy,local}(Y,t). \tag{27}$$

2.5. Algorithm verification

2.5.1. The angular velocity of a single particle in a Couette flow

To confirm the wall effect, the rotation of a single particle in a Couette flow was investigated for varying ratios of channel height to particle radius, H/R. The angular velocity of the particle at the centerline was calculated. The solvent density and the kinematic viscosity were set to $\rho = 1$ and $\nu = 0.1$. For solid particles, the diameter was $D = 20$ ($R = 10$), and the density was $\rho_p = 1$. The height of the channel H was 25 - 300, and the size of the simulation domaion was $400 \times (H + 2)$. For the upper and lower walls, the wall boundary condition was imposed at a shear rate of $\dot{\gamma} = 5 \times 10^{-6}$.

In Fig. 2.1, the equlibrium angular velocity of a particle ω is plotted as a normalized one which was divided by the shear rate at the wall. When the ratio of the channel height to particle radius H/R is low, the normalized ω was less than 0.5 due to the strong influence of the wall. As the channel height is increased, the flow disturbance by the wall is reduced, and the normalized angular velocity converges to 0.5. This result coincides well with Taylor's analytical solution [46] and that of Kromkamp *et al*. [19] by LBM. From this result, we could confirm that the wall height $H = 400$ is appropriate to minimize the wall effect in our system.

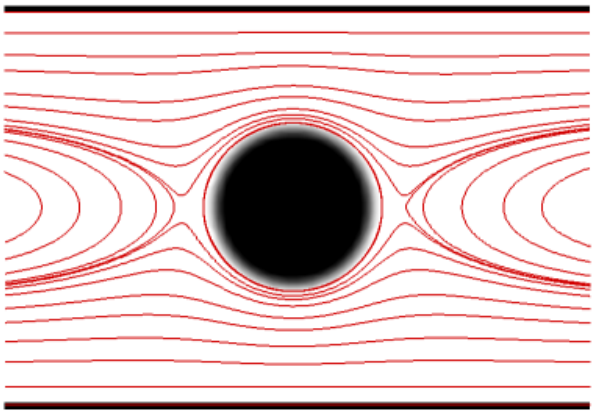

(a)

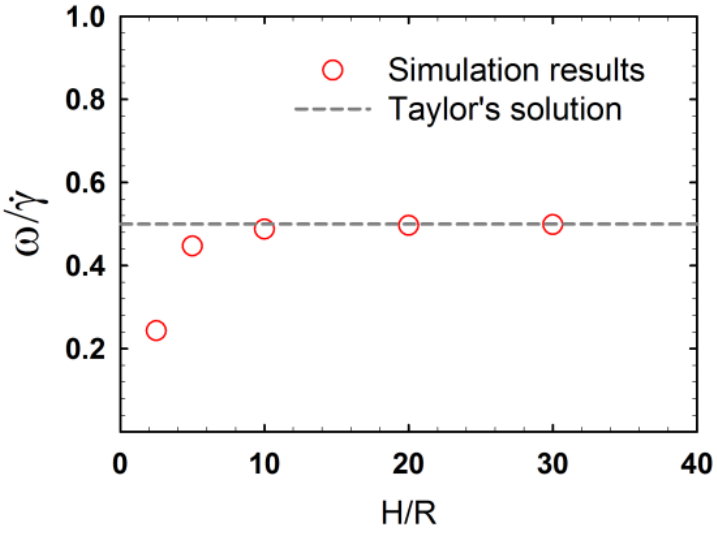

(b)

Fig. 2.1. (a) Streamlines around a single particle in Couette flow for $H / R = 5$. (b) Normalized angular velocity for different ratio of channel height to particle radius, H / R.

2.5.2. The lubrication force between two particles

In concentrated particle suspensions, the role of short range hydrodynamic interaction (HI), or the lubrication force among the particles becomes imporatant [10-13].

To confirm the reproducibility of the lubrication force in the present LBM coupled with SPM, the lubrication force between two spheres (3D case) and two cylinders (2D case) moving toward each other at a constant speed was computed in a rectangular channel. The density of the solvent and particle was $\rho = 1$ and $\rho_p = 1$, respectively. Verification was performed at fixed particle Reynolds number, $\mathrm{Re} = U_{12}(2R)/\nu = 0.2$ with a constant relative velocity for two approaching particles, $U_{12} = (U_1 - U_2) = 0.001$. The size of the simulation domain was set to $4R \times 2R \times 2R$ (R = 2.5 - 10 in 3D case) and $4R \times 2R$ (R = 5 - 20 in 2D case), respectively. A periodic boundary condition was imposed on all boundaries, and the tests were peformed with varing particle radii, R, to confirm the dependency of the lattice resolution in our algorithm.

In the 3D system, the lubrication force F_{lub} for the two approaching particles was calulated by simulation, and it was comapared with the analytical solution from Eq. (28) [47-49].

$$\frac{F_{\mathrm{lub}}}{2\rho\nu U_{12}/\lambda} = \frac{3\pi}{4s} + C_w. \tag{28}$$

For two spherical particles with the same radius, λ was defined as $1/R$, and s was $d/R - 2$, where d means the center to center distance between the particles. C_w is a constant which depends on the wall, and $C_w = 0$ was used under the assumption of

an infinite channel height. As shown in Fig. 2.2(a), the result coincides well with the theoretical prediction in the 3D system. A 2D simulation was also performed. The F_{lub} values obtained by the simulation are plotted with the analytical solution of Dodd *et al.* [50] in Fig. 2.2(b). The simulation results matched well with the analytical solution. These results confirm that the lubrication force between two particles (or cylinders) is well represented in SPM-LBM.

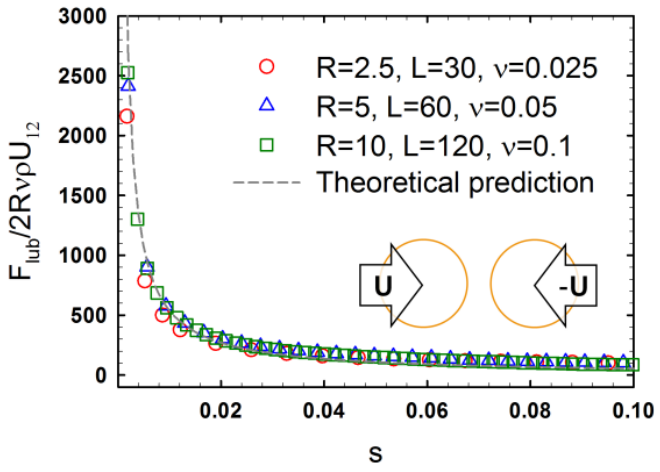

(a)

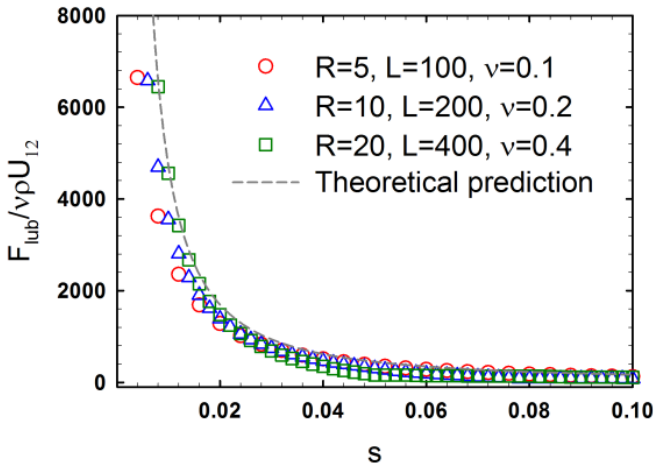

(b)

Fig. 2.2. (a) Lubrication force between two identical spheres (3D) for different particle radius, *R*. The dashed line was obtained from the lubrication theory, Eq. (27). (b) Lubrication force between two identical cylinders (2D) for different particle radius, *R*.

2.5.3. Local shear stress of a single particle measured by MOP algorithm

To verify the MOP algorithm in LBM coupled with SPM, a preliminary test was performed as follows. The stress of a single particle placed at the center of a confined channel was measured by both WSS and MOP. The simulation domain was 100 × 102 (including wall nodes), and the solid particle diameter was set as D = 20. The dimensionless relaxation parameter τ was set to unity, and the kinematic viscosity was set as $\nu = 1/6$. The moving wall boundary condition in Eq. (20) was imposed for the upper and lower wall with a shear rate of $\dot{\gamma} = 10^{-4}$, and the periodic boundary condition was applied to the flow direction.

As shown in Fig. 2.3(a), a shear stress developed in the simulation domain, and high stress was generated around a particle. The stress distribution for both the solvent and particle was measured by MOP, and it was plotted in terms of channel height H shown in Fig. 2.3(b) together with the result of the WSS. At the center of the channel where the single particle was located, the stress contribution by the particle phase was dominant, and the total stress coincided well with that of the WSS. As verified by this result, the stress contribution from both the solvent and particle was well decomposed, and the local stress could be measured successfully in the present LBM coupled with SPM and MOP

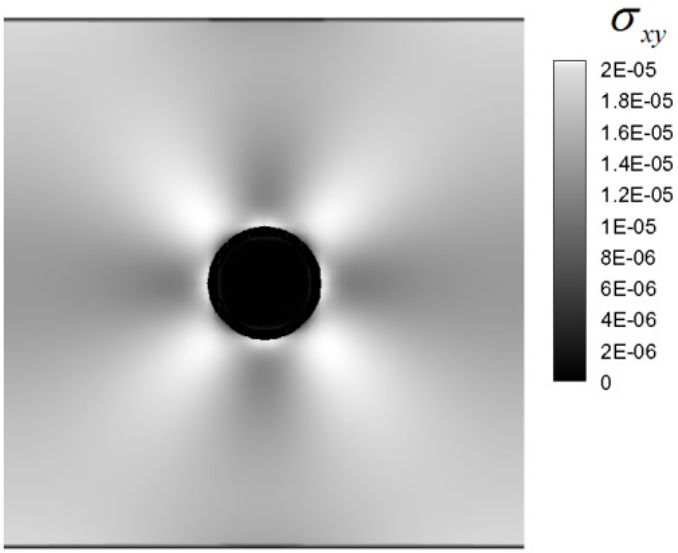

(a)

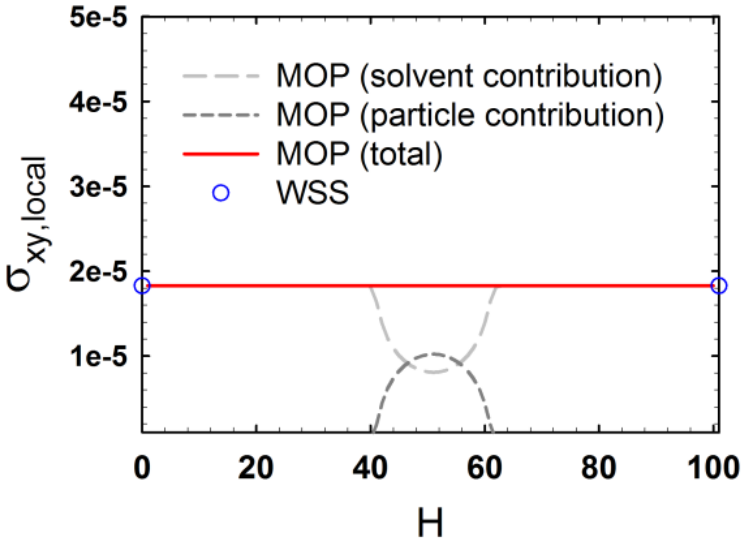

(b)

Fig. 2.3. (a) Distribution of shear stress around a single particle and (b) stress distribution as a function of channel height, *H*.

Chapter 3. Results and discussion

3.1. Shear thickening of non-Brownian suspensions in confined channel

3.1.1. Simulation setup

In this study, LBM was adopted as a solvent solver, and SPM was coupled with LBM to describe the motion of particles that had a hydrodynamic interaction.

A solvent density of $\rho = 1$, dimensionless relaxation time of $\tau = 0.8$, and kinematic viscosity of $\nu = 0.1$ were used. For solid particles, a non-Brownian particle was assumed, and the particle diameter and particle density were set to $D = 20$ and $\rho_p = 1$. These material properties correspond to a real solvent system with a density of 1,000 kg/m^3, kinematic viscosity of $v = 10^{-6}$ m^2/s and to real hard-sphere particles with a diameter of 20 μm and a density of 1,000 kg/m^3. In this case, the lattice unit length and unit time are $\Delta x = 1\mu$m and $\Delta t = 0.1\mu$s, respectively. The simulations were performed for suspensions with the following particle volume fractions and numbers of solid particles: $\phi = 0.1$, 0.2, 0.3, 0.4, 0.5 and 0.6, and 49, 100, 156, 204, 255 and 306, respectively. The size of the simulation domain was 400 × 402 (width × height, including wall nodes), and the channel height was 400, which corresponds to 400 μm in a real system. It is large enough compared to the particle diameter of 20 μm, and it is quite similar to the usual gap size of 500μm - 1000μm in the rotational rheometer in real experiments.

Moving wall boundary conditions were imposed to both the upper and lower walls, and the periodic boundary condition was used in the flow direction.

3.1.2. Relative shear viscosity at low particle Reynolds number

We investigated the viscosity at a particle Reynolds number of $Re_p = 0.01$, for which the inertia can be neglected. Re_p means the ratio of the inertia force to the viscous force on a solid particle, and it is defined by Eq. (29).

$$\mathrm{Re_p} = \frac{\dot{\gamma} D^2}{\nu}. \tag{29}$$

The Mach number Ma was kept below 0.1 for a stable calculation under an incompressible fluid assumption [51]. It was defined by Eq. (30), where H denotes the channel height.

$$\mathrm{Ma} = \frac{\dot{\gamma} H}{2 c_s}. \tag{30}$$

The initial velocity was set to zero, and the shearing wall boundary condition was adopted. As shown in Fig. 3.1, the shear flow was imposed in the simulation domain, and the shear stress induced by the interaction between the solid particles and solvent was monitored. The enhanced shear stress was captured for the higher particle volume fraction shown in Figs. 3.1(d)-3.1(f).

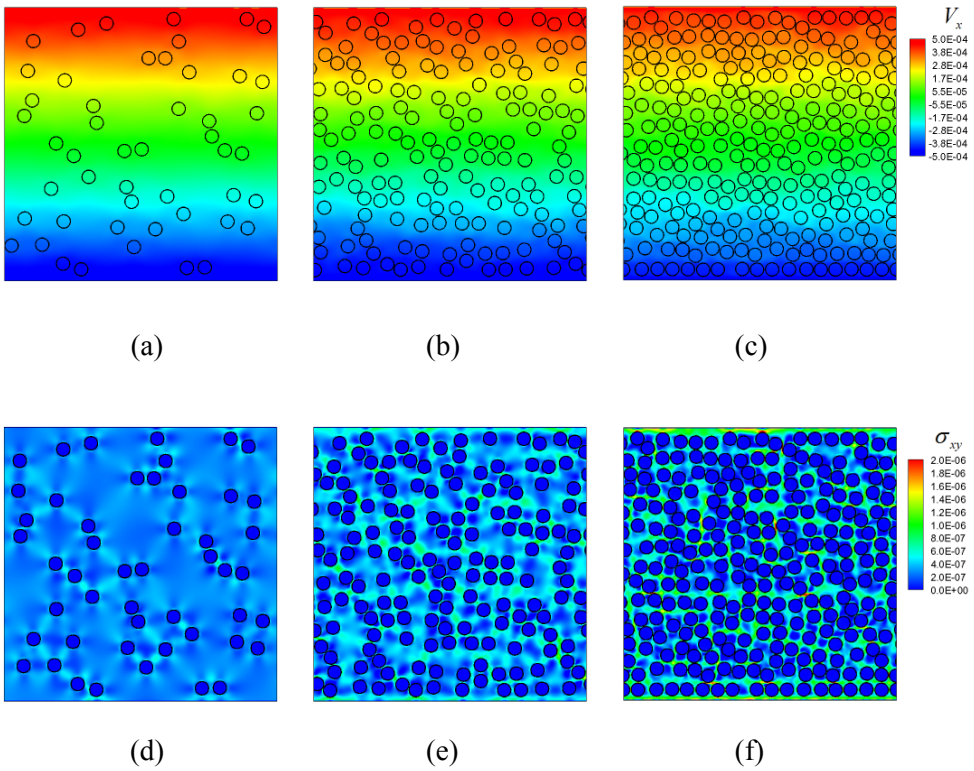

Fig. 3.1. x-component of velocity and shear stress (of the solvent) at time step 300,000 ($Re_p = 0.01$). (a)-(c) denote particle configurations with x component of velocity in color for $\phi = 0.1$, $\phi = 0.3$ and $\phi = 0.5$. (d)-(f) show the distribution of shear stress (of the solvent) for $\phi = 0.1$, $\phi = 0.3$ and $\phi = 0.5$.

Next, the shear viscosity of the suspension was quantitatively analyzed for varying particle volume fractions. To measure the shear stress, both wall shear stress (WSS) and the method of planes (MOP) were used. Calculations were performed for 300,000 time steps in each case, and the shear stress was obtained by averaging over 200,000 of the final time steps, where the stress reached a steady-state with some fluctuations. We also performed simulations for 4,000,000 time steps, and found that the results (shear stress, viscosity, and local density distribution) are basically the same. Thus we will provide the results only for 300,000 time steps. The shear stress was measured only at the wall in the WSS case; however, it was obtained by averaging the local shear stress in Eq. (27) over all the planes along the gradient direction in MOP.

The shear viscosity of the suspension was determined by the shear stress divided by the applied shear rate on the system, and the relative shear viscosity was defined as a ratio of the suspension viscosity and solvent viscosity shown in Eq. (31).

$$\eta_r = \frac{\eta_{suspension}}{\eta_{solvent}}. \tag{31}$$

Because the shear viscosity was determined in terms of the wall shear rate, it could well be regarded as an apparent shear viscosity.

Nonhomogeneous shear rate is known to develop in the concentrated suspension in the confined system due to the absence of particles near the wall region [19,20]. The shear viscosity which is defined according to the bulk shear rate can be different from the apparent shear viscosity (~1 % for $Re_p = 0.01$, ~20 % for $Re_p = 1.0$). The two results may be different to some degree, but the trend itself

does not change at all. Therefore, we will use wall shear rate to define the shear viscosity in this study.

The relative shear viscosity is plotted in Fig. 3.2. For both WSS and MOP, the relative viscosity showed an overshoot followed by a decrease and finally reached a steady-state. The results are the same at long times for both cases.

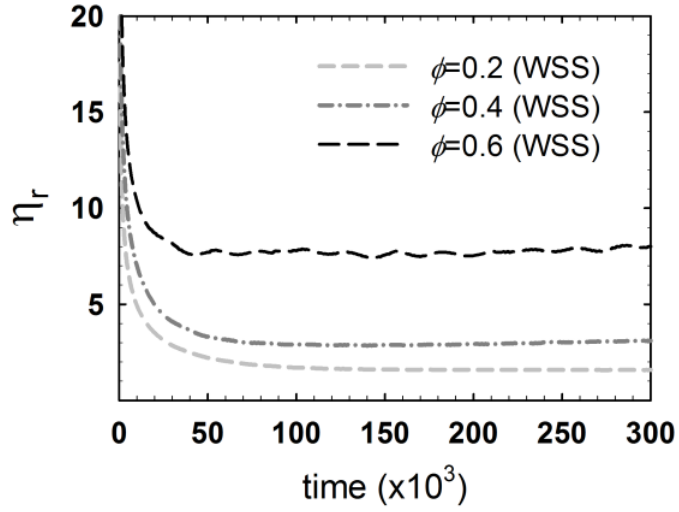

(a)

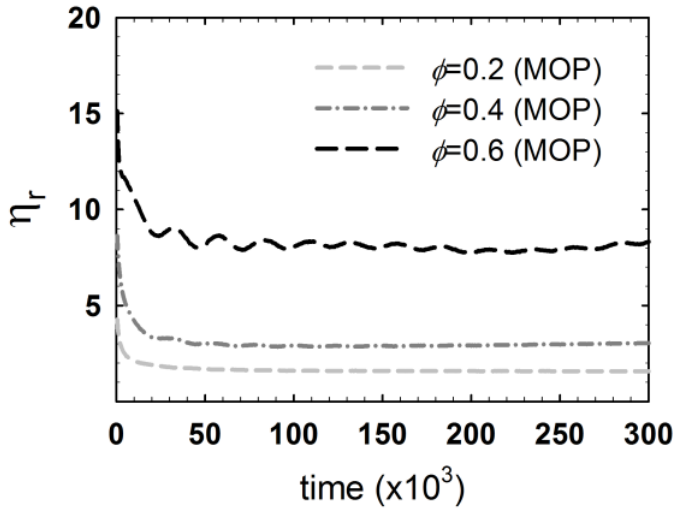

(b)

Fig. 3.2. Relative shear viscosity at different volume fraction of solid particles (Re_p = 0.01). (a) WSS and (b) MOP.

The relative shear viscosity can often be predicted by the Krieger-Dougherty equation, Eq. (32), which is a well-known semiempirical model for a particle suspension [52].

$$\eta_r^{KD} = \left(1 - \frac{\phi}{\phi_{\max}}\right)^{-[\eta]\phi_{\max}} . \tag{32}$$

In Eq. (32), ϕ is the overall particle volume fraction; $\phi_{\max}$ is the maximum packing fraction, and the dimensionless factor $[\eta]$ denotes the intrinsic viscosity of the suspension. In this study, $\phi_{\max} = 0.88$ and $\phi_{\max}\,[\eta] = 1.82$ were used as in previous experimental and simulation reports [19,53]. Even though the experiment was carried out with 3D particles, it was applicable to both the 2D and 3D suspensions at low Reynolds number as shown in Kromkamp *et al*. [19].

The relative shear viscosity as a function of the particle volume fraction is plotted in Fig. 3.3. It was evaluated by both WSS and MOP, and the result was obtained by averaging five simulation sets with different initial configurations of solid particles. An increase in the relative shear viscosity was observed with an increase in the particle volume fraction, and the results corresponded well with the Krieger-Dougherty equation for both WSS and MOP. It means that LBM coupled with SPM can be applied to investigate the rheology of particle systems from dilute to concentrated suspensions. Furthermore, it also proves that MOP can be used as an alternative approach to measure the rheological properties in LBM coupled with SPM.

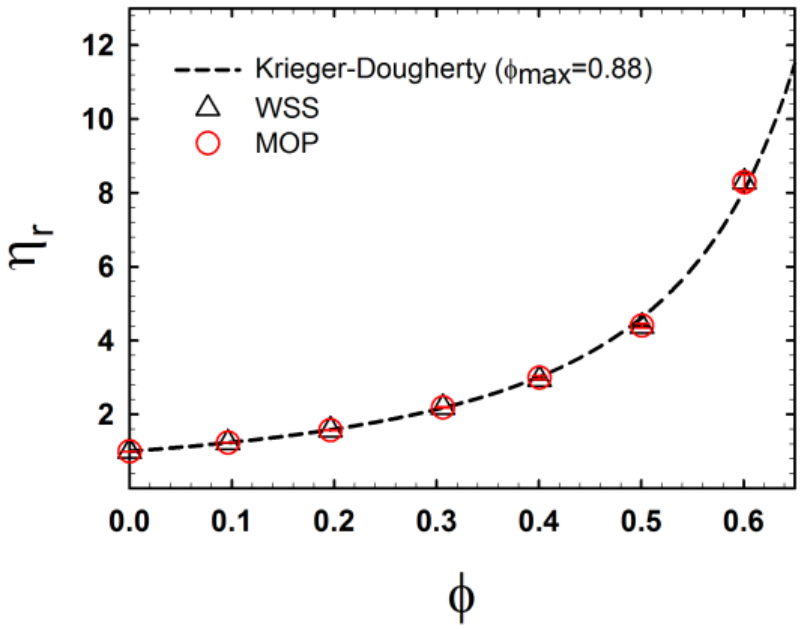

Fig. 3.3. Relative shear viscosity in terms of volume fraction of solid particles ($Re_p = 0.01$). Error bar was obtained by averaging the data from 200,000 to 300,000 time steps (for five simulation sets). Both algorithms (WSS and MOP) predict the Krieger-Dougherty equation very well.

3.1.3. Shear thickening at high particle Reynolds number

The rheology of concentrated particle suspensions (ϕ = 0.3-0.6) was investigated at high particle Reynolds number. Re_p was only controlled by the shear rate, and the other simulation parameters were the same as in Section 3.1.2.

The relative shear viscosity was obtained through the same process as in the previous section, and is plotted in Fig. 3.4. For all the cases, a strong overshoot was observed at first, and it decreased to equilibrium at around 100,000 time steps. Even though there exists a discrepancy at the initial stage, the predictions by MOP and WSS coincided well for a large strain. In WSS, the shear stress is measured only at the wall boundary, while the shear stress is averaged from the local shear stress obtained at each plane in MOP. This difference may lead to a slightly different stress, especially at the initial stage when the momentum is not fully transferred to the domain.

The increase in the relative shear viscosity at a high shear rate, the so-called shear thickening, was captured with an increase in Re_p; however, the growth rate was different for different volume fractions. For ϕ = 0.4 shown in Figs. 3.4(a) and 3.4(b), a small difference was observed for Re_p = 0.01 and Re_p = 1.0, but for more concentrated suspensions of ϕ = 0.5 and 0.6, a highly enhanced relative shear viscosity was observed at high Re_p seen in Figs. 3.4(c)-3.4(f).

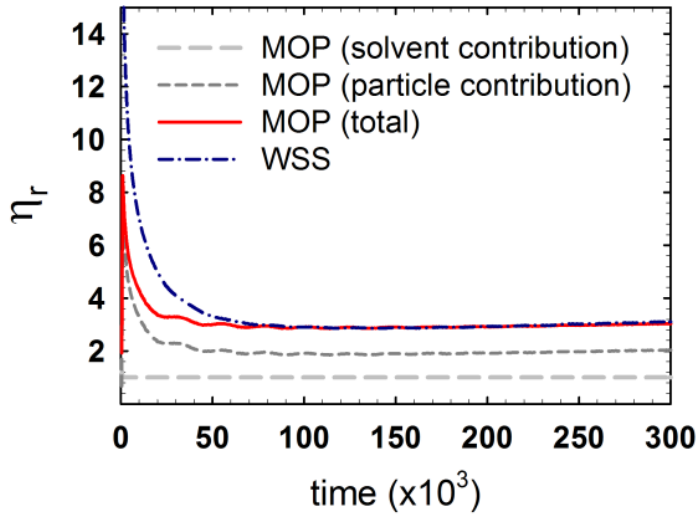

(a)

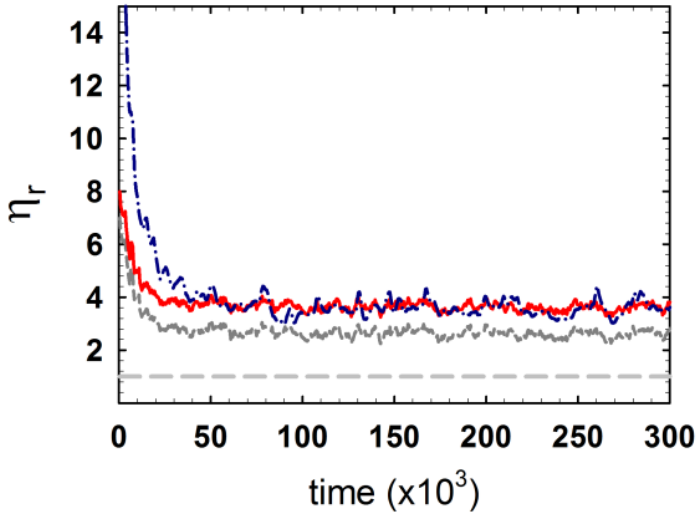

(b)

Fig. 3.4. Relative viscosity measured by wall shear stress (WSS) and by the method of planes (MOP): (a) $\phi = 0.4$, $Re_p = 0.01$; and (b) $\phi = 0.4$, $Re_p = 1.0$.

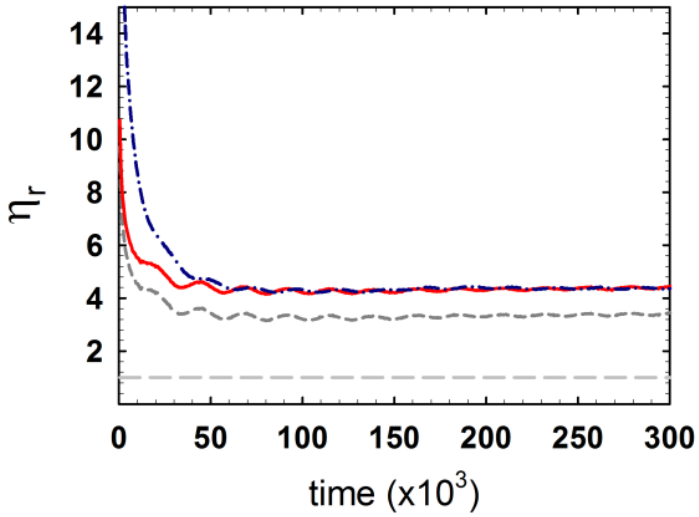

(c)

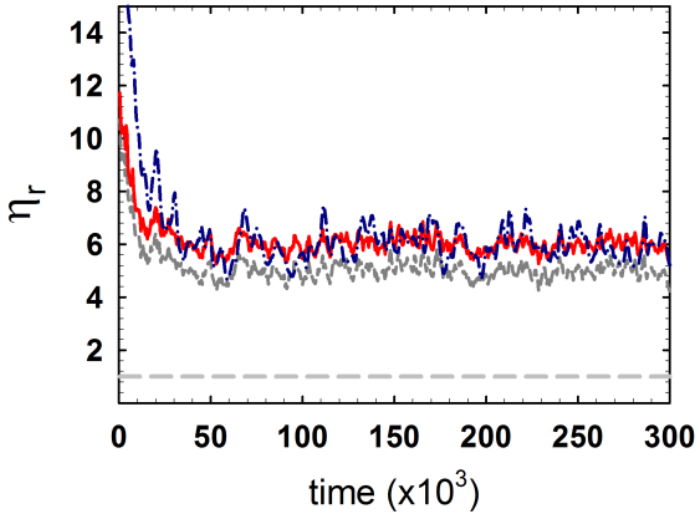

(d)

Fig. 3.4. Relative viscosity measured by wall shear stress (WSS) and by the method of planes (MOP): (c) $\phi = 0.5$, $Re_p = 0.01$; and (d) $\phi = 0.5$, $Re_p = 1.0$.

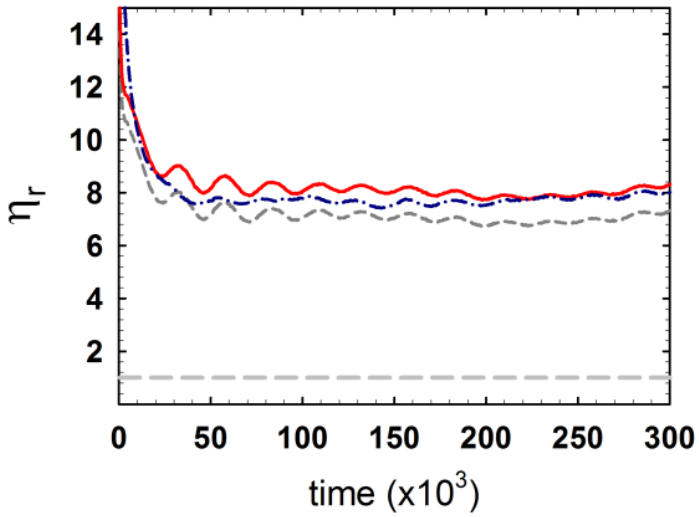

(e)

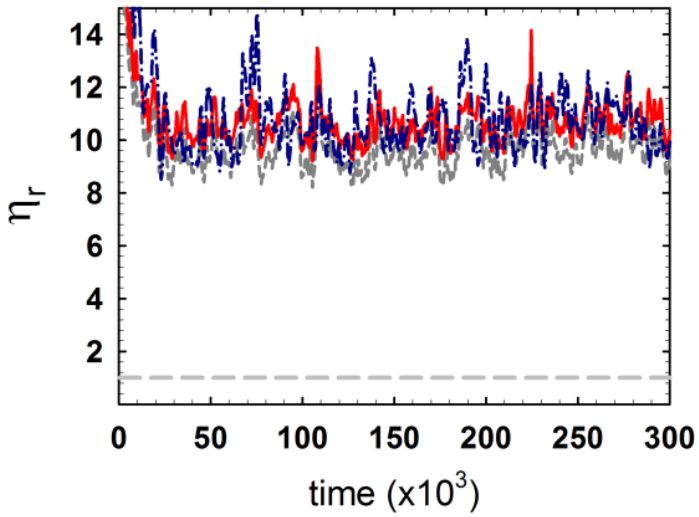

(f)

Fig. 3.4. Relative viscosity measured by wall shear stress (WSS) and by the method of planes (MOP): (e) $\phi = 0.6$, $Re_p = 0.01$; and (f) $\phi = 0.6$, $Re_p = 1.0$.

The total relative shear viscosity showed a strong fluctuation with time, especially in the shear thickening region for both WSS and MOP. When we separated the contribution of each phase, only the particle contribution showed a strong fluctuation in the shear thickening region, in which the solvent contribution was constant at 1.0 shown in Figs. 3.4(b), 3.4(d), and 3.4(f). These results prove that the fluctuation in the total relative shear viscosity originates from the particle contribution. It could be that shear thickening is strongly correlated with the microstructural evolution of the suspension under large deformation as in previous reports [12,13] which will be discussed in the next section.

In Fig. 3.5, the relative shear viscosity is plotted in terms of Re_p. The increase in shear viscosity and shear thickening was clearly captured, and the results by both WSS and MOP coincided well with each other. In Table 2, the values for the relative shear viscosity are compared. At $\phi = 0.3$, the difference in the relative shear viscosity at $Re_p = 0.005$ and $Re_p = 2.0$ was 0.3059 (WSS) and 0.2958 (MOP). In this case, both results from WSS and MOP were well matched, but shear thickening was not strong. However, for higher particle volume fractions of $\phi = 0.4$-0.6, shear thickening was more pronounced. Differences in the shear viscosity between $Re_p = 0.005$ and $Re_p = 2.0$ was as follows: for $\phi = 0.4$, 0.8387 (WSS) and 0.8146 (MOP); for $\phi = 0.5$, 1.9798 (WSS) and 1.9985 (MOP), and for $\phi = 0.6$, 4.4340 (WSS) and 4.5485 (MOP).

It is well known that shear thickening is more pronounced for more concentrated and higher shear rate systems [9,12,17], and our simulation corresponds well with previous experimental and numerical studies. Furthermore, the results obtained by both WSS and MOP match well with each other, which also means that we can use MOP as an alternative method to measure the shear stress

(or shear viscosity) in LBM coupled with SPM.

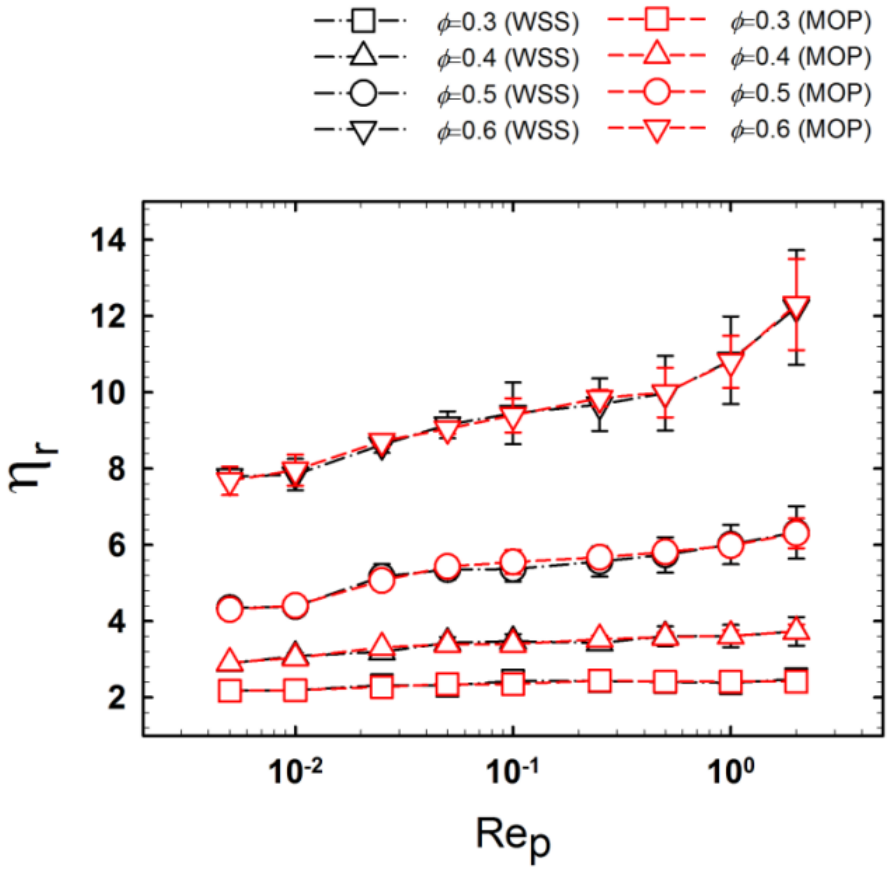

Fig. 3.5. Shear viscosity as a function of particle Reynolds number. Increase of relative shear viscosity was observed at high particle Reynolds number Re_p. The results from WSS and MOP are matched well with each other (error bar was obtained by time average from 200,000 to 300,000 time steps for five simulation sets which have different initial particle configurations).

Table 2

Relative shear viscosity which was measured by wall shear stress (WSS) and the method of planes (MOP).

	$Re_p = 0.005$	$Re_p = 0.01$	$Re_p = 0.1$	$Re_p = 1.0$	$Re_p = 2.0$
$\phi = 0.3$ (WSS)	2.1762	2.1897	2.4356	2.3819	2.4821
$\phi = 0.4$ (WSS)	2.8945	3.0826	3.4766	3.6098	3.7332
$\phi = 0.5$ (WSS)	4.3476	4.3854	5.3655	6.0123	6.3274
$\phi = 0.6$ (WSS)	7.7917	7.8427	9.4512	10.8428	12.2257
$\phi = 0.3$ (MOP)	2.1747	2.1905	2.4452	2.4130	2.4705
$\phi = 0.4$ (MOP)	2.9120	3.0404	3.3956	3.6146	3.7266
$\phi = 0.5$ (MOP)	4.3043	4.4066	5.5489	5.9823	6.3028
$\phi = 0.6$ (MOP)	7.6391	7.9973	9.4619	10.7896	12.1876

3.1.4. Microstructure

In the previous section, the shear viscosity was evaluated by both the WSS and MOP. Shear thickening was successfully captured, but the origin of the shear thickening is still less clear. Therefore, we tried to explain shear thickening from a microstructural change in the suspensions.

First, the pair distribution function for the particle configuration was investigated in the shear-gradient (x - y) plane because the non-Newtonian behavior of the particle system is closely related with the anisotropy in the pair distribution function [13]. The pair distribution function for $\phi = 0.6$ at various particle Reynolds numbers is plotted in Fig. 3.6. In Fig. 3.6(a), the pair distribution function at low Re_p ($Re_p = 0.01$) is plotted. In this case, a strong intensity to the flow direction is clearly observed, which means that most particles are aligned to the flow direction under the shear flow. If the system is dominated by the Brownian motion, the particle alignment is suppressed by self-diffusion, and the isotopic pair distribution function is obtained [12]. However, an anisotropic particle distribution was observed even at low Re_p as small as 0.01 because our system corresponds to the hydrodynamics dominant region where the Brownian motion is negligible. As shown in Figs. 3.6(b) and 3.6(c), a more orientated structure to the compressive axis was observed at high Re_p. In other words, more particles were aligned to the compressive axis at a higher shear rate. It is well known that the structural change of the particles is related with non-Newtonian behavior such as shear thinning and shear thickening [12,13]. In particular, the particle alignment in the compressive axis was strongly correlated with shear thickening in hard-sphere suspensions, which was well explained by the simulation studies with Stokesian dynamics (SD).

In this regard, our simulation confirms the results of previous reports.

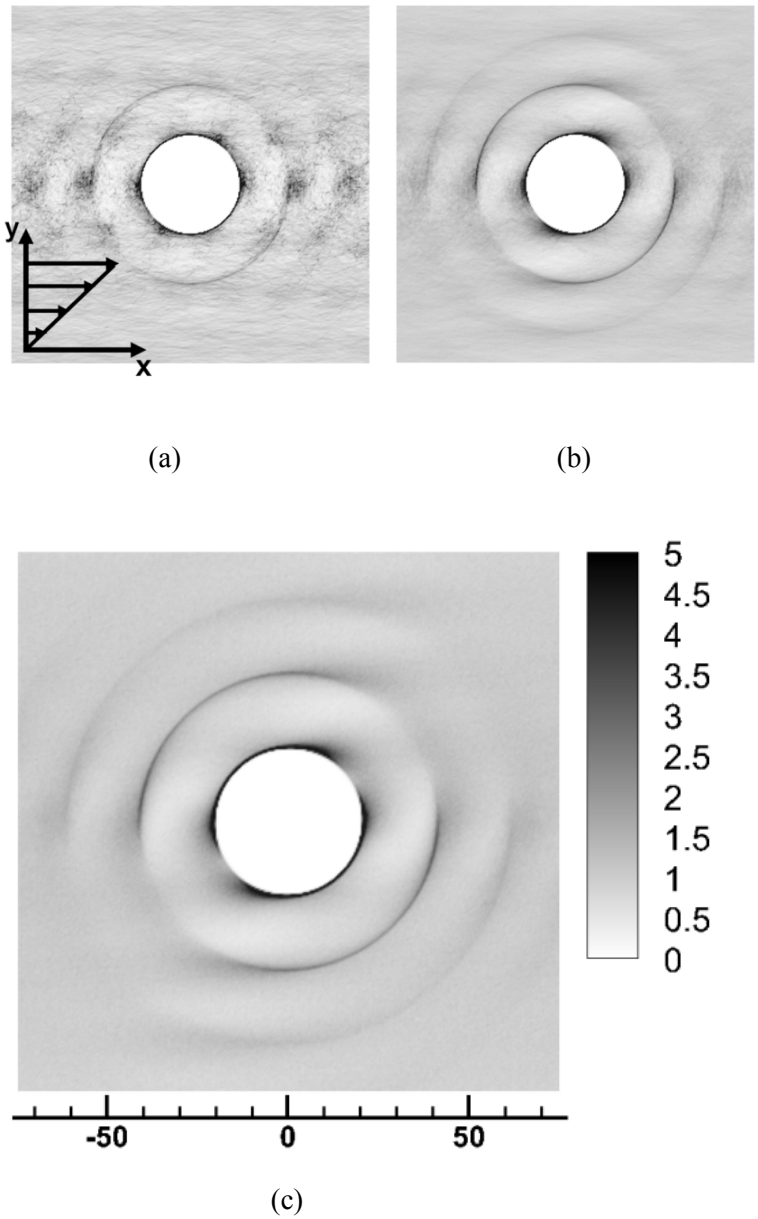

Fig. 3.6. Time averaged pair distribution function for $\phi = 0.6$. (a) $Re_p = 0.01$, (b) $Re_p = 0.01$ and (c) $Re_p = 1.0$. Abscissa denotes flow direction and ordinate denotes gradient direction. Darker region represents higher probability to find particles.

The increase in particle distribution in the compressive axis means that the particles come closer in that direction, which facilitates the formation of clusters [10]. The relationship between shear thickening and particle clusters has been widely reported in both experiments [7-9] and numerical studies [10,11,18]. D'Haene *et al*. observed particle clustering in the shear thickening region by rheo-optical studies [7]. Cheng *et al.* reported a particle structure in both shear thinning and shear thickening regimes [9]. They directly observed cluster formation along the compressive axis in a shear thickening regime by fast confocal microscopy, and they confirmed that shear thickening is related with the size of the clusters at a high Peclet number. Brady and Bossis [11] related shear thickening of Brownian hard-sphere suspensions with particle clustering, which are the so-called hydro-clusters in a suspension. They argued that more clusters can be formed by a strong lubrication force among the particles at a high Peclet number, which leads to shear thickening. Raiskinmäki *et al.* [18] investigated shear thickening of non-Brownian suspensions by LBM, and reported a relationship between the probability of the clustering of particles and the shear thickening intensity. They confirmed that the number of clusters as well as their size increases with Re_p in the shear thickening region. Even though previous studies dealt with systems with minor differences between each other, they all concluded that the formation of clusters can trigger shear thickening in suspensions.

We also carried out an analysis to confirm the relationship between shear thickening and cluster formation. In our analysis, a cluster was defined as a group which has more than one bond among the particles. The bond was counted when the surface to surface distance of the particles was lower than 4% of the particle diameter, which was determined from the first peak in the pair distribution of the

particles. The particle configuration at time step 300,000 is plotted in Fig. 3.7. The particles included in the same cluster were marked with the same color. Here, the particles with a red color denote the ones belonging to the largest cluster, while the particles with a blue color are the individual particles which are not included in the cluster. As seen in Fig. 3.7, a small amount of clusters was formed at $Re_p = 0.01$ even at a high particle volume fraction, but more clusters were observed at higher Re_p. In particular, in the case of $\phi = 0.6$ in Figs. 3.7(c) and 3.7(f), the formation of a larger cluster is clearly observed with the increase in Re_p. At the same time, most clusters aligned in the compressive axis, which explains qualitatively well the anisotropy in the pair distribution function shown in Fig. 3.6.

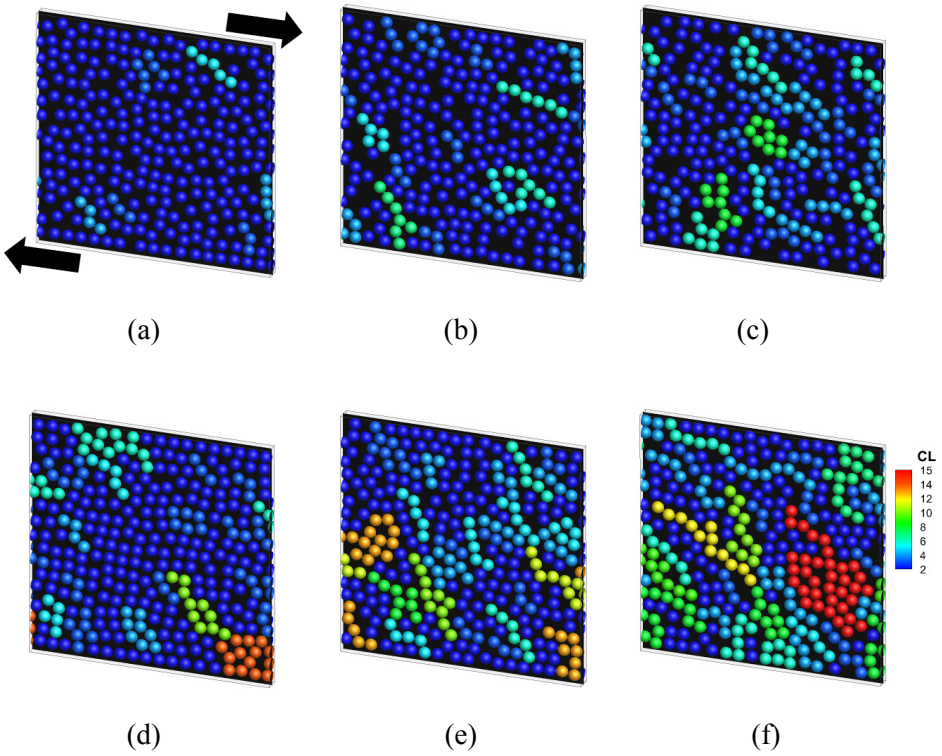

Fig. 3.7. Particle configuration at time step 300,000. (a) $\phi = 0.5$, $Re_p = 0.01$; (b) $\phi = 0.5$, $Re_p = 0.1$; (c) $\phi = 0.5$, $Re_p = 1.0$; (d) $\phi = 0.6$, $Re_p = 0.01$; (e) $\phi = 0.6$, $Re_p = 0.1$; and (f) $\phi = 0.6$, $Re_p = 1.0$. The particles in the same cluster have the same color. Nonclustering particles are blue, and the particles in the larger cluster are closer to red.

The size distribution of the clusters was quantitatively analyzed too. Here, the number of particles N and the probability P_N were calculated to find clusters that consist of N particles. The results were obtained by averaging the values from the simulation time 200,000 to 300,000 for five simulation sets with different initial configurations. Graphs in terms of P_N and N are shown in Fig. 3.8. In Fig. 3.8(a) where $\phi = 0.4$, only a small amount of clusters was formed even at high Re_p, but more clusters were observed at a higher volume fraction. This was more pronounced at higher Re_p shown in Fig. 3.8(b). The increase in cluster size at high Re_p was in accordance with the shear thickening behavior in Fig. 3.5, which coincides well with previous reports from both experiments [7-9] and simulation studies [10,11,18]. Especially, the increase in cluster distribution is qualitatively similar to the results of Cheng *et al*. [9]. Even though they studied Brownian suspensions, both results show a resemblance in terms of the formation of clusters in the hydrodynamic force dominant region.

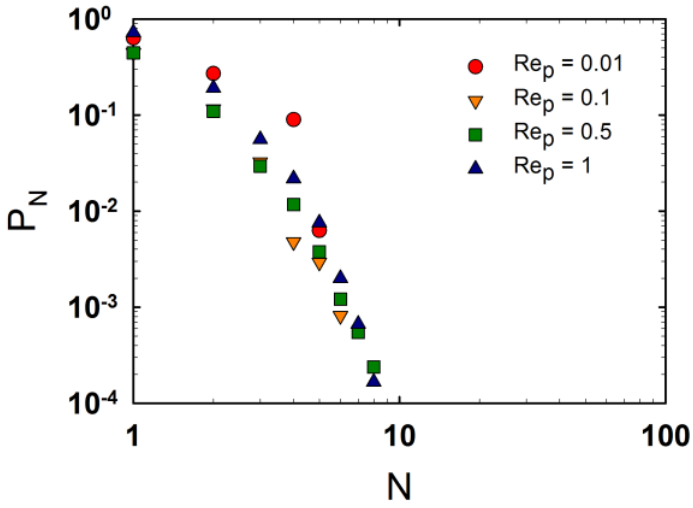

(a)

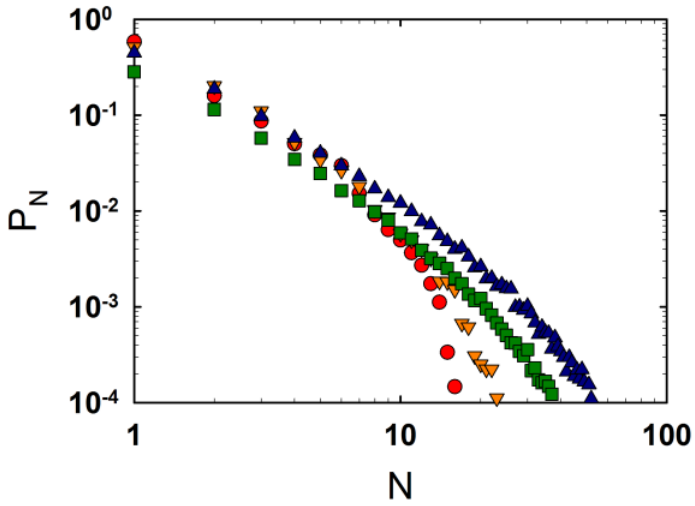

(b)

Fig. 3.8. Time averaged probability of the number of solid particles in clusters. (a) $\phi = 0.4$ and (b) $\phi = 0.6$. Larger clusters were formed with an increase in particle Reynolds number at higher volume fraction.

The orientation of clusters was also checked in terms of the angular distribution of the particles which are included in the clusters. The angle between two particles in cluster θ was calculated by Eq. (33) in terms of the center to center distance r_{ij} and the y component of the vector $X_{i,y} - X_{j,y}$ for the i and j particles.

$$\theta = \tan^{-1}\left(\frac{X_{i,y} - X_{j,y}}{r_{ij}}\right). \tag{33}$$

Time averaged probability is plotted in Fig. 3.9. Here, P_θ denotes the angular distribution of the particles within a cluster. A $\theta < 90°$ describes a region of extension, and a $\theta > 90°$ means a region of compression in the flow direction. For $\phi = 0.4$, the distribution was lower than that of $\phi = 0.6$ shown in Fig. 3.8, and the angular distribution increased at higher Re_p for all the cases. For a more concentrated system such as $\phi = 0.6$, an increase in the distribution was clearly observed, which means that more particles were aligned in the compressive axis with clustering. This can be related to the particle alignment which was described in Figs. 3.6 and 3.7, and it also coincides with previous reports in both experiments [9] and numerical studies [10-12,20].

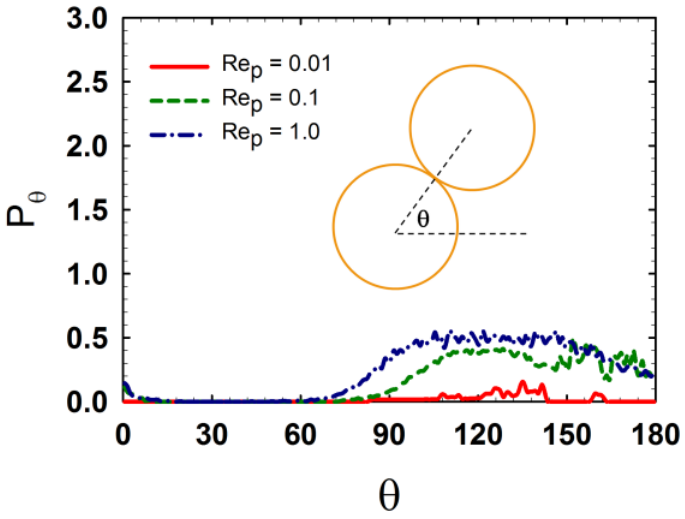

(a)

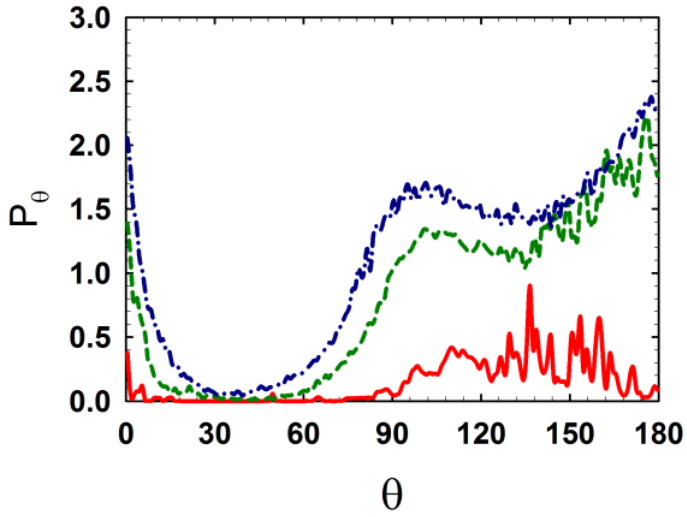

(b)

Fig. 3.9. Time averaged angular distribution of clusters. (a) $\phi = 0.4$ and (b) $\phi = 0.6$. Higher angular distribution was observed over 90°, which means that the clusters are aligned to the compressive axis.

3.1.5. Analysis of local shear stress and local particle volume fraction

As already mentioned, shear thickening is closely related to the increase in clusters at high particle Reynolds number Re_p. The bulk rheology is strongly affected by the structural change of the suspension, especially by the formation of clusters. However, it is still unclear how the local structure of the material affects the local rheology, and changes the bulk rheology. There exist few reports on the correlation between local rheology and local structure of a suspension because it is hard to directly measure the local rheology of a material either by experiments or by simulation due to many technical limitations.

We adopted the method of planes (MOP) [30] which was recently introduced to access the local dynamics of a suspension. In our system, the shear stress in each plane along the gradient direction was defined as the local shear stress [30,45], and it was obtained by the summation of the shear stress of solvent and that of the particles which was locally measured by Eq. (23)-(27).

First, the time averaged solvent and particle contributions to the total shear stress were locally calculated along the channel height, and the results are compared with WSS in Figs. 3.10(a) and 3.10(b). Here, we described the local shear stress as normalized by the shear rate at the moving wall $\dot{\gamma}_{\mathrm{wall}}$ multiplied by the solvent viscosity η_0. Under the assumption that the local shear rate is the same with the shear rate near the wall, the normalized shear stress can be explained as the relative shear rate. The time averaged local shear stress by MOP coincided well with that measured by WSS, and shear thickening at high Re_p was also captured. In the particle contribution measured by MOP, a fluctuation exists near the wall, which might be correlated with the density distribution of the particles near the wall.

To confirm this, the particle volume fraction was locally measured. The local particle volume (area in 2D) fraction was calculated by the smoothed profile function in Eq. (5). After summing the smoothed profile functions at the LBM nodes in each plane, it was divided by the surface area (length in 2D) of each plane. Then, the local particle volume (area) fraction in each plane could be obtained.

The time averaged local particle volume (surface area in 2D system) fraction is plotted in Figs. 3.10(c) and 3.10(d) in terms of the channel height H. For all the cases, a strong concentration fluctuation was observed near the wall, and it looks qualitatively similar with the results in previous experimental [9] and simulation studies [17,19,20]. The fluctuation of the local particle volume fraction in Figs. 3.10(c) and 3.10(d) was well reflected in the particle contribution to the local shear stress shown in Figs. 3.10(a) and 3.10(b), and these results show how MOP captures the local shear stress upon microstructural changes. We now focus on the local shear stress at specific times because the local rheology could be constantly changing due to the structural evolution of the suspension during the flow. The data at simulation time step 300,000 were chosen as representative for which the cluster formation was clearly captured with shear thickening shown in Fig. 3.7.

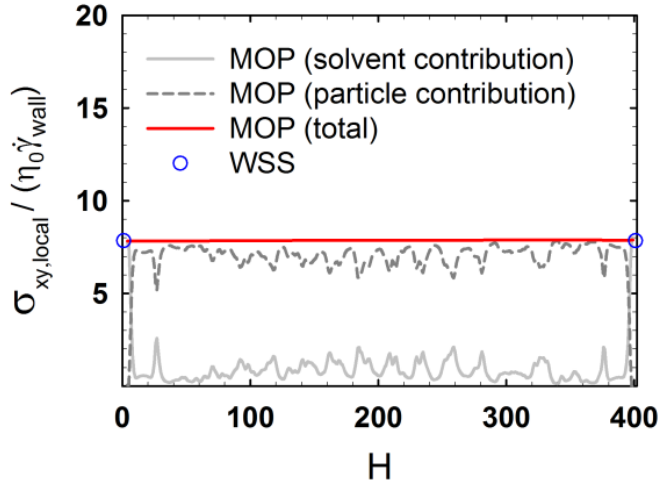

(a)

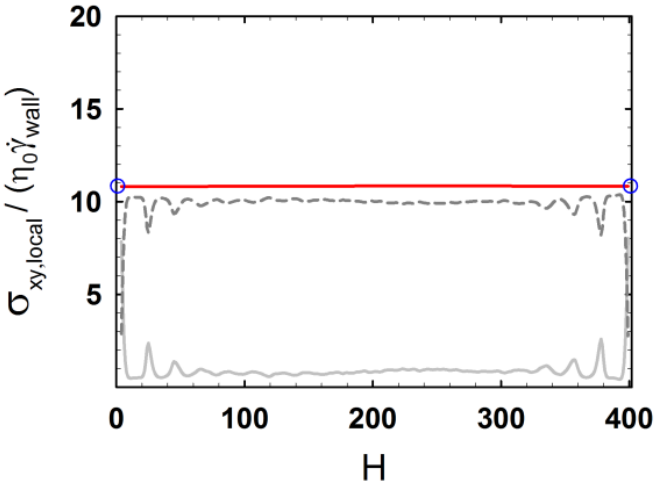

(b)

Fig. 3.10. Time averaged (from 200,000 to 300,000) local shear stress measured by the method of planes (MOP) to the gradient direction for $\phi = 0.6$: (a) $Re_p = 0.01$ and (b) $Re_p = 1.0$.

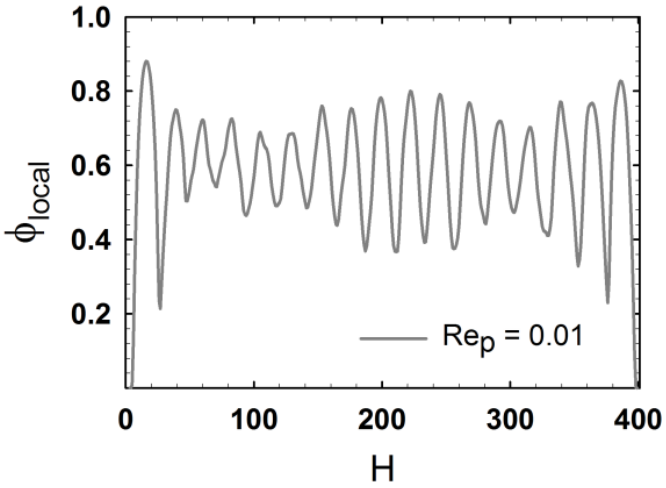

(c)

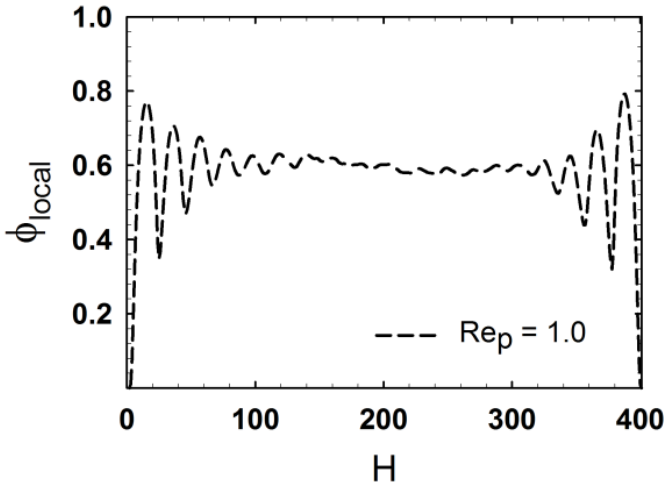

(d)

Fig. 3.10. Time averaged (from 200,000 to 300,000) local particle volume (area) fraction: (c) $Re_p = 0.01$ and (d) $Re_p = 1.0$.

The normalized local particle stress (the particle contribution in local shear stress) and local particle volume fraction at time step 300,000 are plotted in Fig. 3.11. At high Re_p, an increase in the local shear stress was observed, and this was enhanced for a more concentrated system and for higher Re_p shown in Fig. 3.5. Of note is the correlation between the local shear stress and local particle volume fraction. At low Re_p where shear thickening did not occur, the fluctuation for both the local shear stress and local particle volume fraction looks similar shown in Figs. 3.11(a), 3.11(c), and 3.11(e). However, as seen in Figs. 3.11(b), 3.11(d), and 3.11(f), the correlation between the local shear stress and local volume fraction decreased at high Re_p (Re_p = 1.0), which is more clearly observed at a higher particle volume fraction.

Correlations between the local shear stress and the local particle volume fraction can be quantitatively analyzed by Pearson's correlation coefficient [54]. It is denoted as r_{corr} and is defined by Eq. (34). Here, $\phi_{i,local}$ and $\sigma^{p}_{xy,i,local}$ mean the local particle volume fraction and the local particle stress in plane i, and $\bar{\phi}_{local}$ and $\bar{\sigma}^{p}_{xy,i,local}$ are the averaged values over all the planes.

$$r_{corr} = \frac{\sum(\phi_{i,local} - \bar{\phi}_{local})(\sigma^{p}_{xy,i,local} - \bar{\sigma}^{p}_{xy,i,local})}{\left[\sum(\phi_{i,local} - \bar{\phi}_{local})^2 \sum(\sigma^{p}_{xy,i,local} - \bar{\sigma}^{p}_{xy,i,local})^2\right]^{0.5}}. \tag{34}$$

When the linear correlation is strong, r_{corr} is close to 1, and it reduces to 0 when there is no correlation.

The Pearson's correlation coefficient r_{corr} between the local particle stress and the local volume fraction is plotted in Fig. 3.12. For ϕ = 0.4, r_{corr} was 0.9022 at Re_p = 0.01 and 0.8838 at Re_p = 1.0. There exists a strong linear correlation, even though

it slightly decreases at high Re_p. For more concentrated suspensions, a reduction of r_{corr} was observed. In the case of $\phi = 0.5$, r_{corr} was 0.8720 at $Re_p = 0.01$ and 0.8239 at $Re_p = 1.0$. In the case of $\phi = 0.6$, r_{corr} was 0.7946 at Re = 0.01 and 0.7040 at $Re_p = 1.0$. It clearly shows that a linear correlation between the local particle stress and the local particle volume fraction decreases for more concentrated suspensions at a high shear rate.

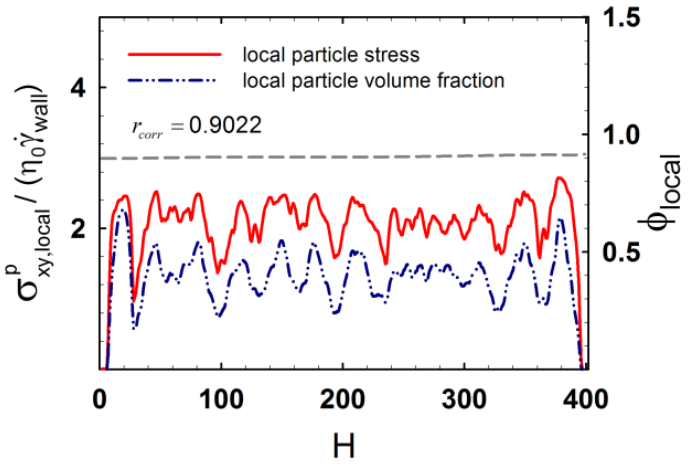

(a)

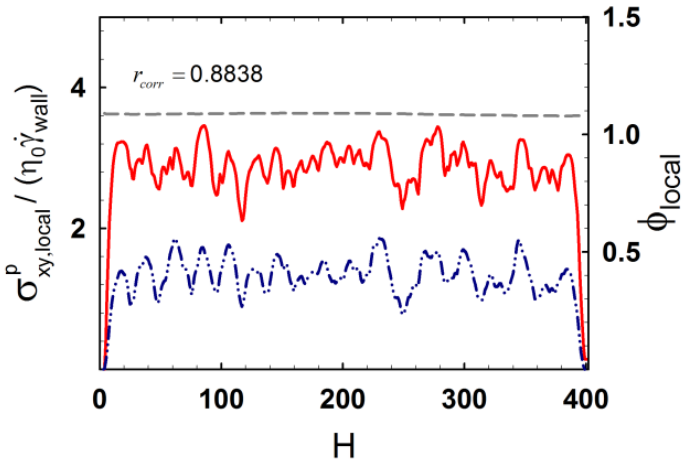

(b)

Fig. 3.11. Local particle stress and local particle volume fractions at t = 300,000. (a) ϕ = 0.4, Re_p = 0.01; and (b) ϕ = 0.4, Re_p = 1.0. Dashed line (grey color) denotes time averaged local stress (total) which was normalized by the shear viscosity of pure solvent multiplied by wall shear rate.

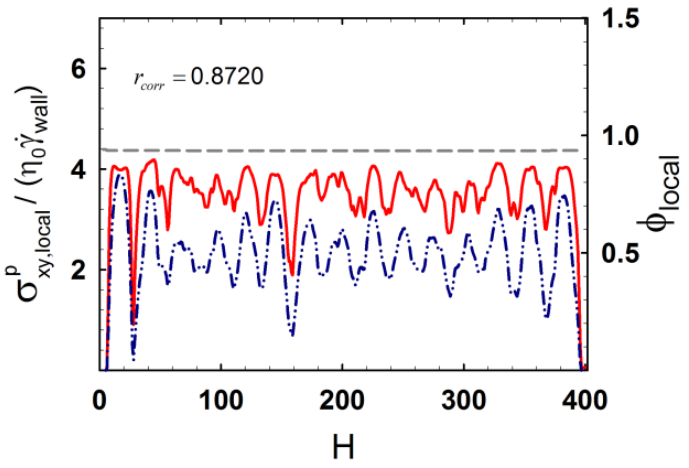

(c)

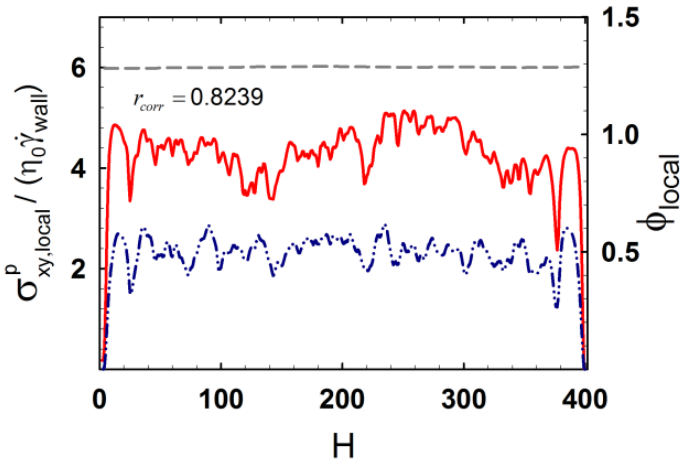

(d)

Fig. 3.11. Local particle stress and local particle volume fractions at t = 300,000. (c) ϕ = 0.5, Re_p = 0.01; and (d) ϕ = 0.5, Re_p = 1.0.

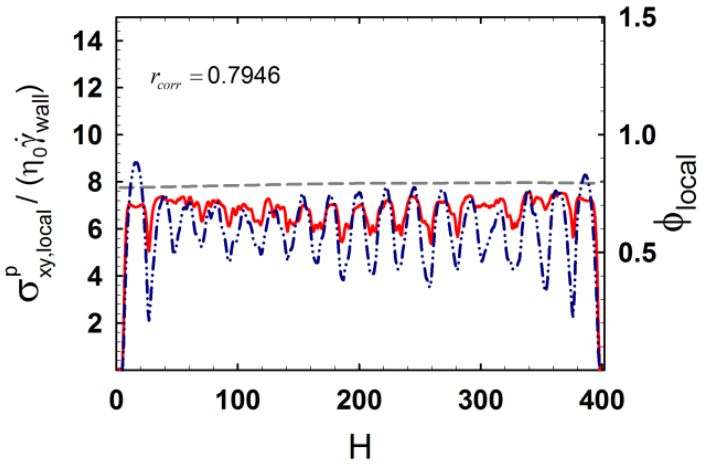

(e)

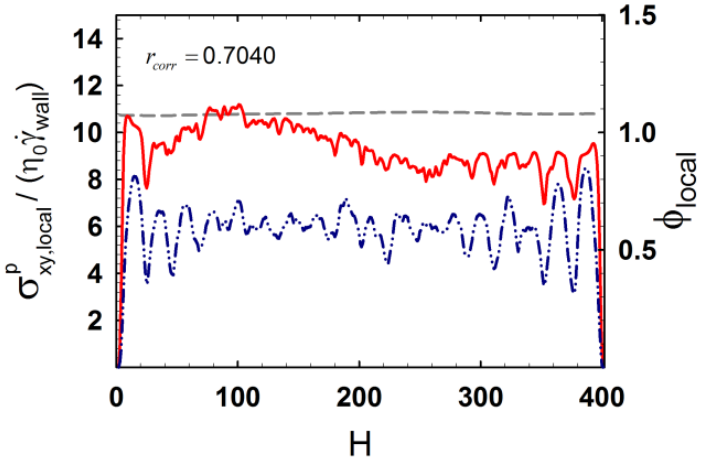

(f)

Fig. 3.11. Local particle stress and local particle volume fractions at t = 300,000. (e) $\phi = 0.6$, $Re_p = 0.01$; and (f) $\phi = 0.6$, $Re_p = 1.0$.

For every 2,000 time steps, the correlation between the local particle stress and the local particle volume fraction was calculated by Eq. (34), and r_{corr} is plotted as a function of time in Fig. 3.12. At the initial stage, a low r_{corr} was observed for all the cases; however, it gradually increased after some time. A low r_{corr} at the initial stage can be understood as the progress of the shear stress (or shear viscosity) growth. As shown in Figs. 3.2 and 3.4, viscosity overshoot was predicted at the initial stage, and then, it equilibrated after enough strain. This could be related with the sudden momentum exchange near the wall boundary in LBM, and this is also verified in r_{corr} in Fig. 3.12. The increase of r_{corr} looks proportional to the particle volume fraction because the probability to form clusters increases due to the reduced distance among the particles. At low Re_p, a relatively high r_{corr} was observed with weak fluctuation, but the decrease of r_{corr} was observed at high Re_p with a strong fluctuation. The fluctuation in r_{corr} looks similar to that in the relative shear viscosity which was shown in Fig. 3.4, and it could be related with the microstructural change, especially cluster formation at high Re_p.

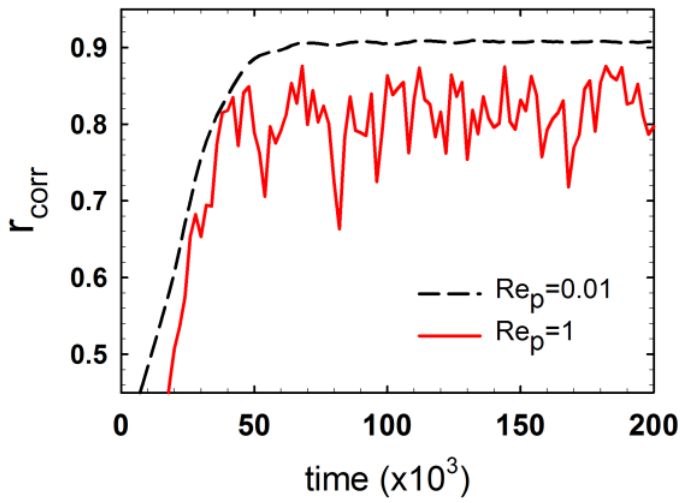

(a)

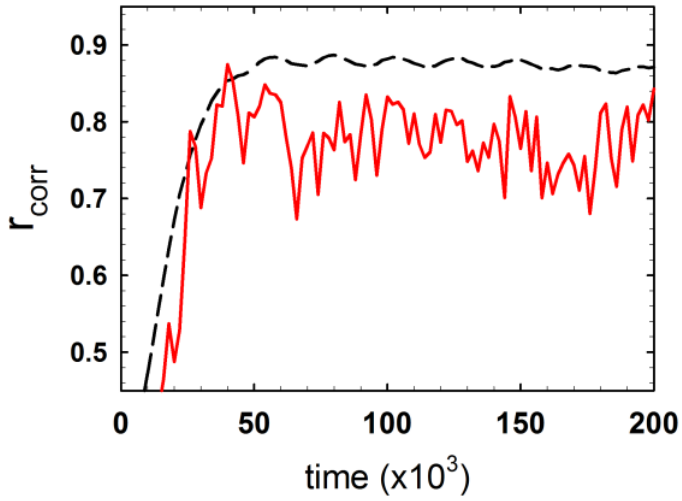

(b)

Fig. 3.12. Pearson's correlation coefficient between local particle stress and local particle volume fractions as a function of time: (a) $\phi = 0.4$ and (b) $\phi = 0.5$.

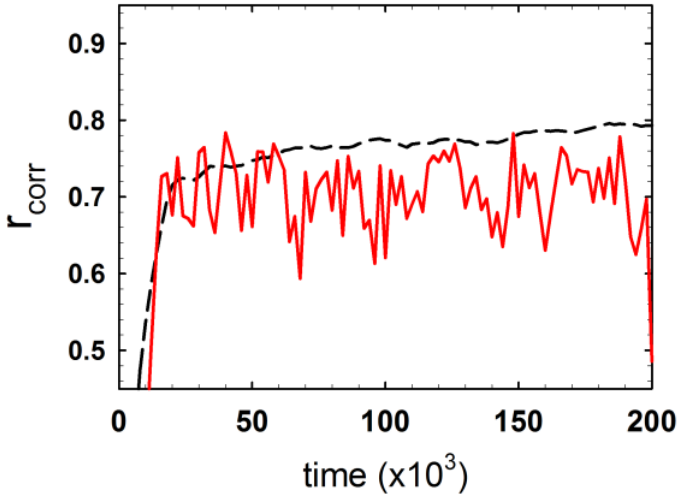

(c)

Fig. 3.12. Pearson's correlation coefficient between local particle stress and local particle volume fractions as a function of time: (c) $\phi = 0.6$.

To more clearly understand the effect of Re_p on the linear correlation between the local particle stress and the local particle volume fraction, the time averaged Pearson's correlation coefficient r_{corr} was plotted as a function of the Re_p in Fig. 3.13. r_{corr} decreased with an increase in the particle volume fraction, and it also decreased with Re_p. When shear thickening was not strong, a slight decrease in r_{corr} was observed at low Re_p, while it showed a sharp decrease at high Re_p with shear thickening. It means that, even though the particles occupied the same amount of space, they can show different rheology depending on their microstructure. Local structural change at higher Re_p could be related with cluster formation shown in Figs. 3.7 and 3.8. It is hard to strictly argue that cluster formation during shear thickening is a key factor in reducing the correlation between the local particle stress and the local particle volume fraction yet, but we could confirm that the local rheology of the suspension that originates from the local microstructural change affects the bulk rheology of the suspension.

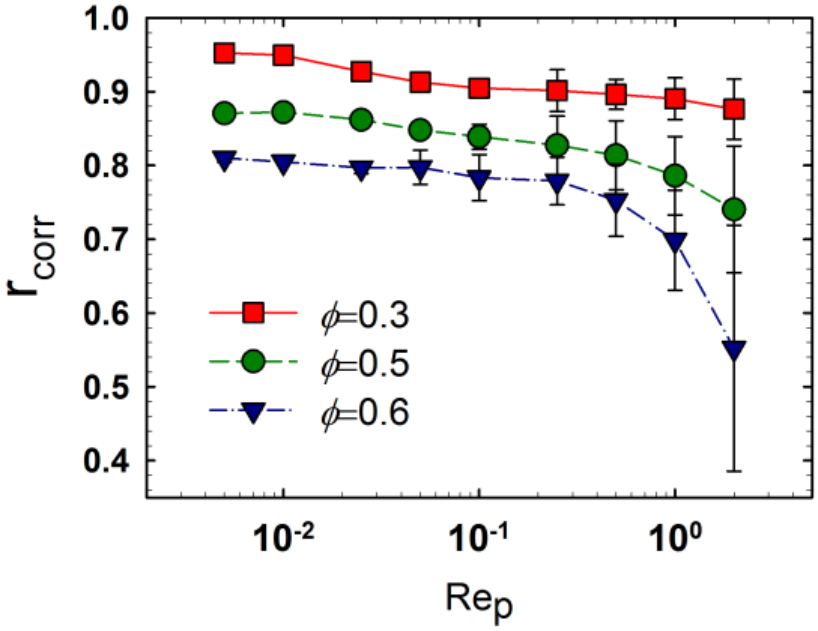

Fig. 3.13. Time averaged Pearson's correlation coefficient between local particle stress and local particle volume fraction. The correlation decreases with the increase in local particle volume fraction and particle Reynolds number, Re_p.

3.2. Strain stiffening of non-Brownian suspensions in liquid and crystal coexistence region

3.2.1. Simulation setup

In this study, the lattice Boltzmann method (LBM) was used as a solvent solver, and the smoothed profile method (SPM) was coupled with LBM to describe solid particles immersed in a solvent. Two-dimensional (2D) non-Brownian suspensions were assumed, and the simulation parameters were set as described below (all variables are denoted in LB units). The solvent density $\rho = 1$ and the dimensionless relaxation time $\tau = 1.1$ (kinematic viscosity $\nu = 0.2$). For solid particles, the particle diameter and particle density were set to $D = 20$ and $\rho_p = 1$, respectively. These material properties correspond to a Newtonian solvent with a density of 1,000 kg/m^3, kinematic viscosity of $\nu = 10^{-6}$ m^2/s, and non-Brownian hard-sphere particles with a diameter of 100μm and a density of 1,000 kg/m^3 (the lattice unit length and unit time are $\Delta x = 5\mu$m and $\Delta t = 5\mu$s, respectively).

We modeled the hard-sphere suspension with the particle volume fraction $\phi = 0.75$ (380 solid particles), which corresponds to $\phi = 0.54$ in a 3D suspension (relative to the maximum packing fraction; $\phi_{max,2D} = 0.88$ and $\phi_{max,3D} = 0.63$). The volume fraction $\phi = 0.54$ is within the liquid and crystal coexistence region ($0.494 < \phi < 0.545$), in which the suspensions are known to locally form the closed packing structure under a shear flow [27,55,56].

The size of the simulation domain was 400 × 402 (width × height, including wall nodes), and the channel height was 400, which corresponds to 2,000 μm based on the parameter set given above. It is not only large enough compared to the

particle diameter of 100 μm, but also close to the usual gap size of 1,000μm in the rotational rheometer.

The moving wall boundary condition was used in both the upper and lower walls, and the periodic boundary condition was imposed on the flow direction. The shear rate $\dot{\gamma}$ was applied in the form of Eq. (18) at the wall boundary.

$$\dot{\gamma} = \gamma_0 \omega \cos(\omega t). \tag{18}$$

Here, γ_0 is the strain amplitude; ω is the angular frequency ($\omega = 2\pi f$, f: frequency), and t denotes the simulation time.

The calculations were performed in the range of the strain amplitudes, $\gamma_0 = 0.01$-0.35 at a fixed frequency $f = 10^{-5}$. Imposed angular frequency ω corresponds to $\omega \sim$ 12.5 rad/s in experiments.

In this work, the shear stress was measured by the method of planes (MOP). This algorithm was originally proposed by Todd *et al.* [42] to access local shear stress of the fluids in confined system. Even though it was originally designed for molecular dynamic (MD) simulation, it was extended to LBM by Krüger *et al.* [30]. Because it has advantages in evaluating the local contribution of the solvent and solid particles to the total stress of the suspensions, it has been applied to investigate the rheology of deformable particle suspensions. Details can be found in references [30].

The calculations were performed for 600,000 time steps (6 oscillatory cycles), and five simulation sets with different initial configurations of solid particles were used to guarantee reproducibility. Finally, data from 4 - 6 cycles (400,000 - 600,000 time steps) were used, where the stress signal was stabilized.

3.2.2. Dynamic moduli of the suspension

The shear stress of the suspension was measured by the strain sweep test (γ_0 = 0.01-0.35) at a fixed angular frequency ($\omega \sim 6.28 \times 10^{-5}$). The phase angle δ and the stress amplitude σ_0 were obtained from the calculated shear stress. The storage (G') and loss modulus (G'') were obtained by the following equations.

$$G' = \frac{\sigma_0}{\gamma_0}\cos\delta, \tag{19}$$

$$G'' = \frac{\sigma_0}{\gamma_0}\sin\delta. \tag{20}$$

Dynamic moduli were plotted as a function of the strain amplitude in Fig. 3.14. At the low strain amplitudes ($\gamma_0 < 0.13$), the plateau moduli were observed, but an overshoot began to appear in both dynamic moduli above $\gamma_0 = 0.13$. With the growth of the strain amplitude, an increase in dynamic moduli (the storage modulus in particular) was clearly observed, and we defined the point $\gamma_0 = 0.13$ where the storage modulus started to increase as the critical strain amplitude $\gamma_{0,c}$. Above the critical strain amplitude, the storage modulus increased with the strain amplitude and then decreased at $\gamma_0 = 0.35$ after the maximum. In this simulation, strain stiffening was successfully observed, and this behavior was similar to experiments [21-27]. However, thinning behavior before the strain stiffening was not confirmed in this simulation.

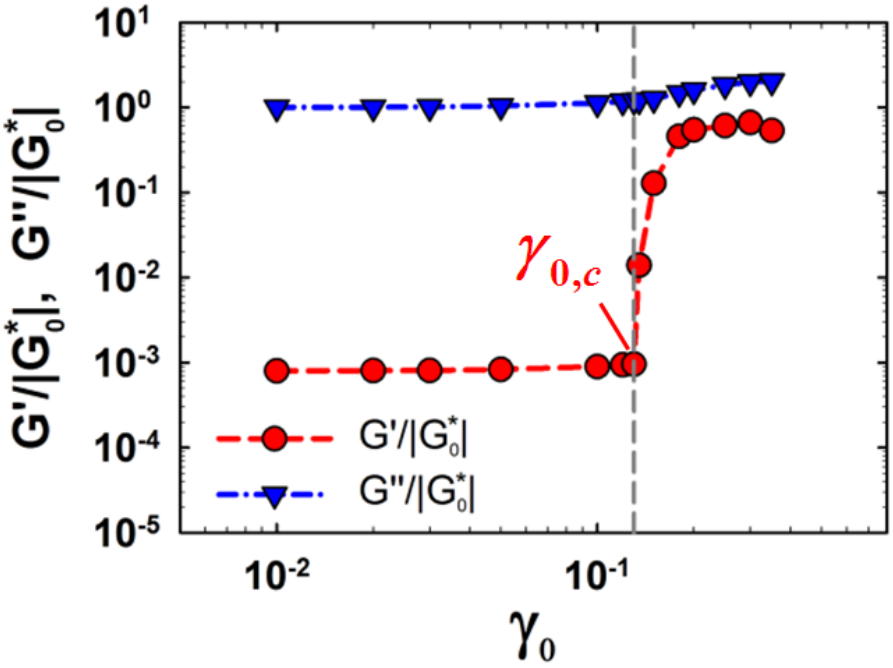

Fig. 3.14. Dynamic moduli as a function of the strain amplitude γ_0 ($\phi = 0.75, f = 10^{-5}$). Both moduli were normalized by the complex moduli at $\gamma_0 = 0.01$ ($|G_0^*|$). Grey vertical line denotes the critical strain amplitude.

3.2.3. Analysis of shear stress waveform

A distorted stress signal has been reported in LAOS for various complex fluids, for example, polymer melts [57-59], polymer blends [60], polymer solutions [61,62], MR (magnetorheological) fluids [63], and concentrated hard-sphere suspensions [64-66]. The shear stresses (normalized by its maximum value) at different strain amplitudes γ_0 are plotted in Fig. 3.15. At the low strain amplitudes below $\gamma_0 = 0.1$, the stress showed a linear sinusoidal signal, but it began to distort over $\gamma_0 = 0.1$. The distortion was enhanced with the increase in the strain amplitude, and a strongly distorted shear stress waveform with a backward tilted pattern was observed at $\gamma_0 = 0.2$. This pattern is quite similar to the experimental results [27], and it could be associated with a significant change in the microstructure of the suspensions [27,57].

The nonlinear response in shear stress can be evaluated by graphical representation (Lissajous curve) which is a closed loop of the shear stress as a function of the strain. In the Lissajous plot, a curve close to a circle is observed in the linear viscoelastic regime, while an elliptic shape is seen in the nonlinear viscoelastic regime [67]. The trends in the Lissajous pattern was also found in our simulation (Fig. 3.15). Contrary to a circular shape at low strain amplitude ($\gamma_0 = 0.01$), it became more elliptic with the increase in the strain amplitude, and the elliptic shape was broken at higher strain amplitudes over $\gamma_0 = 0.2$. Finally, a highly non-elliptical curve began to appear.

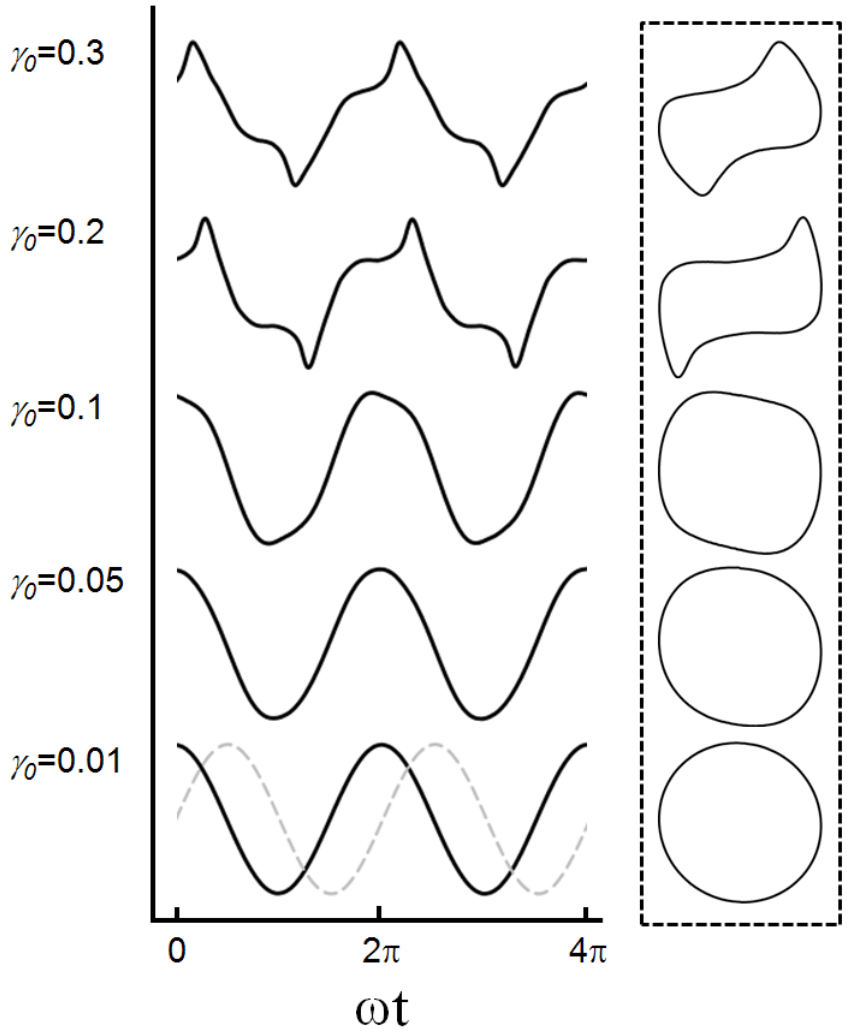

Fig. 3.15. Normalized shear stress (left) and Lissajous curves (right) at various strain amplitudes ($\phi = 0.75$, $f = 10^{-5}$).

Fourier transform (FT) analysis has been widely used to characterize the nonlinear response of various material systems [68-70]. In a linear regime, only the first harmonic appears, n = 1. On the other hand, a nonlinear response appears with the growth of higher harmonic contributions. The relative odd harmonics ($I_{n/1} = I_n / I_1$) were derived, and they are plotted as a function of the strain amplitude in Fig. 3.16. The relative third harmonic ($I_{3/1} = I_3 / I_1$) was investigated first because it is the first and most representative nonlinear parameter. It was very small at strain amplitudes below γ_0 = 0.03 (not shown in the figure), but it increased in the range of γ_0 = 0.03 - 0.2. After reaching the maximum at γ_0 = 0.2, it decreased. It is known that the nonlinearity of the suspensions decreases at large strain amplitudes after a maximum [71], contrary to the asymptotic plateau of polymeric systems [72,73]. Our simulation is in good agreement with previous reports.

The slope (or power index) of $I_{3/1}$ was also investigated. It was obtained by Eq. (21), where a is the intercept, and b is the slope.

$$\log I_{3/1} = a + b \log \gamma_0 . \tag{21}$$

On a log-log diagram, the slope of $I_{3/1}$ was 2.0 in the increasing region (γ_0 = 0.03 - 0.2) and -1.2 in the decreasing region (γ_0 = 0.25 - 0.35). The slope of $I_{3/1}$ at low strain amplitudes was experimentally and theoretically estimated as 2 in polymeric systems [57], but the validity for particle suspensions has yet been established. According to Nam *et al.* [27], the slopes of $I_{3/1}$ were 1.5 and -1.2, respectively. Even though the slope of $I_{3/1}$ in the increasing region was slightly different, the slope in the decreasing region was in good agreement. This means that the simulation predicted the nonlinear response of concentrated suspensions fairly well even for

the dependence of $I_{3/1}$ on the strain amplitude. As shown in Fig. 3.16, the fifth harmonic $I_{5/1}$ and the seventh harmonic $I_{7/1}$ also increased with the increase of the strain amplitude. An interesting point is the sudden change in slopes of $I_{5/1}$ and $I_{7/1}$ near the critical strain amplitude, which means that high order harmonics are associated with the onset of strain stiffening.

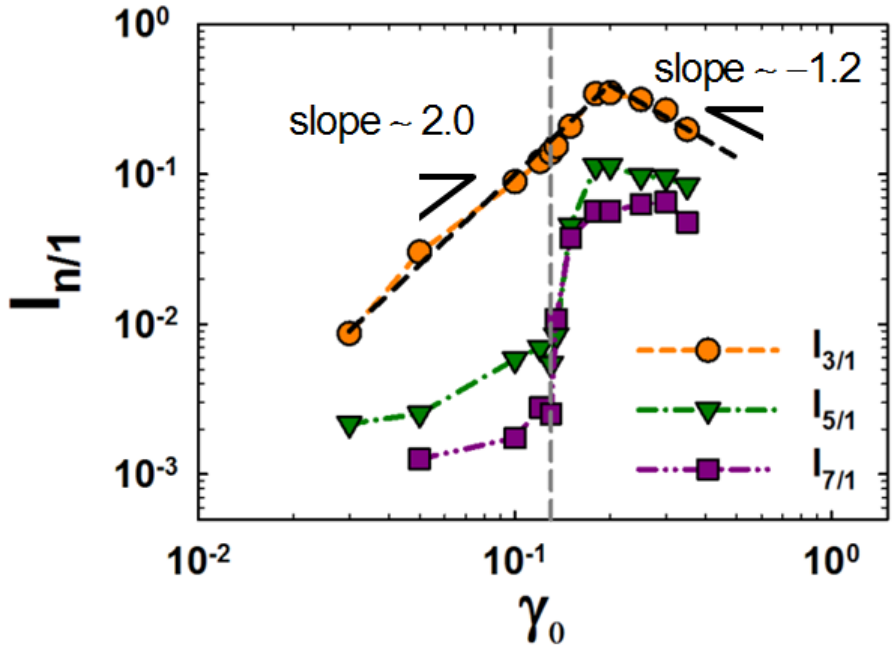

Fig. 3.16. Relative odd harmonics, $I_{n/1}$ versus strain amplitude ($\phi = 0.75$, $f = 10^{-5}$). Grey vertical line denotes the critical strain amplitude $\gamma_0 = 0.13$.

Although FT analysis is useful in quantifying the nonlinear response in LAOS, it is not easy to determine its physical meaning [67]. Therefore, we need other approaches to characterize the nonlinear rheological behaviors. One of the approaches is the stress decomposition, which is a geometric analysis introduced by Cho *et al.* [74]. It was based on the mathematical foundation that the elastic stress σ' should be odd symmetric with respect to the strain and even symmetric with respect to the strain rate, whereas the viscous stress σ'' should be even symmetric with respect to the strain and odd symmetric with respect to the strain rate. In this method, the total stress σ is decomposed in terms of the elastic stress σ' and the viscous stress σ'' as follows.

$$\sigma' = \frac{\sigma(\gamma, \dot{\gamma}) - \sigma(-\gamma, \dot{\gamma})}{2}, \tag{22}$$

$$\sigma'' = \frac{\sigma(\gamma, \dot{\gamma}) - \sigma(\gamma, -\dot{\gamma})}{2}. \tag{23}$$

Cho *et al.* used polynomial regression in their stress decomposition, but it has a limitation in that the material properties are not unique, and they depend on the order of the polynomial which was arbitrarily chosen. Later, the stress decomposition method was extended by Ewoldt *et al.* [67]. In their approach, the use of the Chebyshev polynomial was alternatively suggested, and it was successfully applied to characterize the nonlinear response of various soft materials. In their scheme, the elastic stress and viscous stress were defined by Eq. (24) and (25).

$$\sigma'(x) = \gamma_0 \sum_{n:odd} e_n(\omega, \gamma_0) T_n(x), \tag{24}$$

$$\sigma''(x) = \dot{\gamma}_0 \sum_{n:odd} v_n(\omega, \gamma_0) T_n(y). \tag{25}$$

Here, $x = \gamma / \gamma_0$ and $y = \dot{\gamma} / \dot{\gamma}_0$ provide the appropriate domains of [−1, +1] for orthogonality. $T_n(x)$ denotes the *n*th-order Chebyshev polynomial of the first kind; e_n is the elastic Chebyshev coefficient, and v_n is the viscous Chebyshev coefficient.

Using the stress decomposition method, the elastic stress and the viscous stress were decomposed from the total shear stress, and they are plotted in Fig. 3.17. Note that each stress component was normalized by the maximum total stress obtained at each strain amplitude; therefore, the elastic stress and the viscous stress indicate their relative contributions on the total stress at a specific strain amplitude. As in Fig. 3.17(a), the elastic stress was almost negligible at $\gamma_0 = 0.01$, while the elastic stress showed a peak at the flow reversal (the maximum strain) above $\gamma_0 = 0.15$. The peak grew with the increase in strain amplitude, and finally, it was separated into double peaks at strain amplitudes above $\gamma_0 = 0.17$. Double peaks for the elastic stress were also observed in experiments for hard-sphere suspensions near the liquid and crystal coexistence region [27], and our results successfully reproduced the experimental data. Although the physical meaning of the double peaks is not fully discussed in this work, it was confirmed that our simulation reflects the physics in a real suspension system very well. As observed in Fig. 3.17(b), the elastic stress is even symmetric at the flow reversal (maximum strain), and the distance between the peaks increased with the strain amplitudes.

The maximum of the elastic stress and the viscous stress are plotted in Fig.

3.18(a). Both stress components increased with the increase in strain amplitude, and a sudden slope change was observed near the critical strain amplitude. In Fig. 3.18(b), the normalized stress components by the maximum of the total stress at each strain amplitude are plotted to confirm the relative contribution between the elastic and viscous stress on the total stress. Below the critical strain amplitude, both the elastic and the viscous stress showed a plateau behavior. The increment of the elastic stress was observed near the critical strain amplitude, contrary to the decrease in the viscous stress. This implies that strain stiffening was accompanied by the elasticity enhancement of the suspension under a large amplitude oscillatory shear flow.

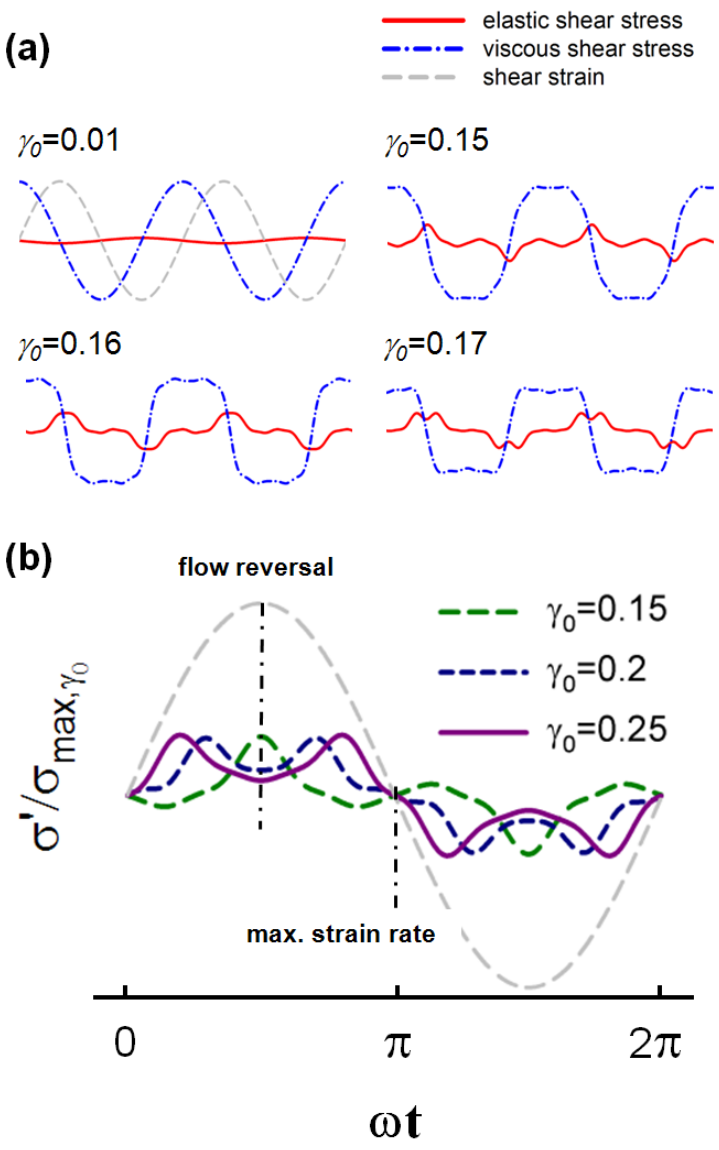

Fig. 3.17. (a) Elastic and viscous stress components which were normalized by the maximum of the total stress at each strain amplitude ($\sigma_{\max,\gamma_0}$). (b) The elastic stress at different strain amplitudes. The grey line is the strain.

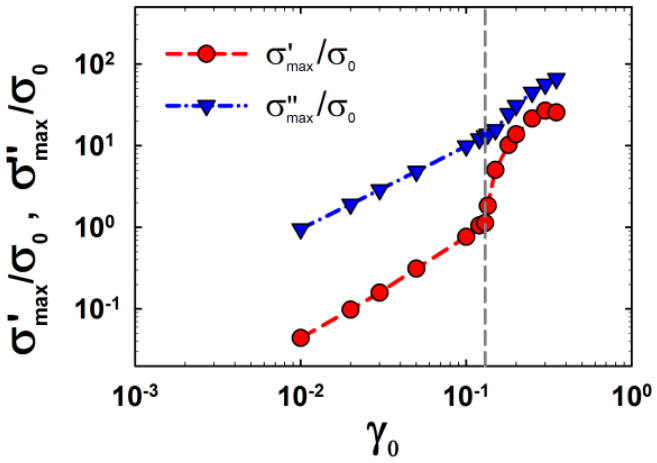

(a)

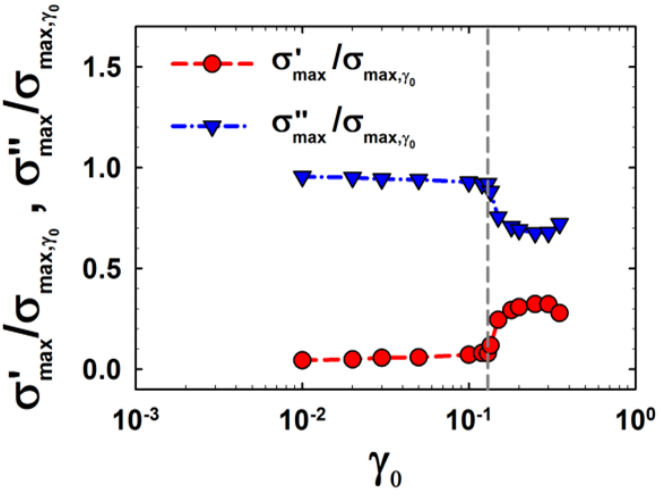

(b)

Fig. 3.18. (a) The maximum stress components which were normalized by the maximum of the total stress at $\gamma_0 = 0.01$ ($\sigma_{max,0}$). (b) The maximum stress components which were normalized by the maximum of the total stress at each strain amplitude (σ_{max,γ_0}). Dashed vertical line denotes the critical strain amplitude.

3.2.4. Microstructure

In the previous section, the nonlinear response of the suspension was analyzed by FT analysis and stress decomposition. Even though they can provide useful information on the nonlinearity of the suspensions, they are not enough to provide a clear understanding on the mechanism of strain stiffening.

It has been reported that the rheological properties of the suspensions are strongly related with their microstructure. For example, the formation of hydroclusters due to the lubrication among the approaching particles was suggested as a key mechanism of shear thickening in a steady shear flow, and this was carefully verified by both experiments and numerical simulations [6-20]. On the other hand, the microstructure of the suspensions has rarely been investigated during strain stiffening, and a few studies only presume that the formation of hydroclusters or the rearrangement of the particles under a dynamic shear flow is the cause of strain stiffening [23,25,27]. Therefore, our goal is to find the origin of strain stiffening of hard-sphere suspensions in the liquid and crystal coexistence region, and for that purpose, the microstructural evolution of the suspension was analyzed.

First, the pair distribution function (PDF) was investigated from the particle configuration in the shear-gradient (x - y) plane. $\gamma_0 = 0.2$, which showed a strongly distorted shear stress, was selected as a representative case for the analysis. The PDF is plotted in Fig. 3.19. Here, $g(r)$ is the probability to find other particles within the center to center distance r, and h denotes a dimensionless distance between the surfaces of two adjacent particles ($h = (r - D) / D$). The PDF at $\omega t = 0$, $\omega t = \pi/2$ (flow reversal) and $\omega t = \pi$ are plotted in Fig. 3.19(a). At $\omega t = 0$, the peaks

of $g(r)$ were observed at specific regions ($h \sim 0.1$, $h \sim 0.9$ and $h \sim 1.2$), and the highest peak appeared at $h \sim 0.1$. The $g(r)$ peak implies that the particles are regularly distributed in a domain within a specific distance, and the highest $g(r)$ peak, which is observed at low h, signifies that most particles maintain close distances. At $\omega t = \pi/2$, the highest $g(r)$ peak appeared at lower h ($h \sim 0.04$), which implies that the average distance of the particles decreased with the increase in strain. The $g(r)$ peak at $\omega t = \pi$ was overlapped with the peaks at $\omega t = 0$, which means that the suspension completely recovers its structure at strain = 0 before and after the flow reversal. On the other hand, $g(r)$ peaks at the transient strain ($\omega t = \pi/4$ and $\omega t = 3\pi/4$) behaved differently. At $\omega t = \pi/4$, the highest peak appeared at $h \sim 0.04$, while the highest peak was at $h \sim 0.1$ at $\omega t = 3\pi/4$. In addition, broad peaks were observed in the region from $h \sim 0.04$ to $h \sim 0.1$ for $\omega t = 3\pi/4$, whose shape was clearly different from the $g(r)$ peaks at $\omega t = \pi/4$. These results indicate that the change in microstructure is asymmetric under the oscillatory shear flow.

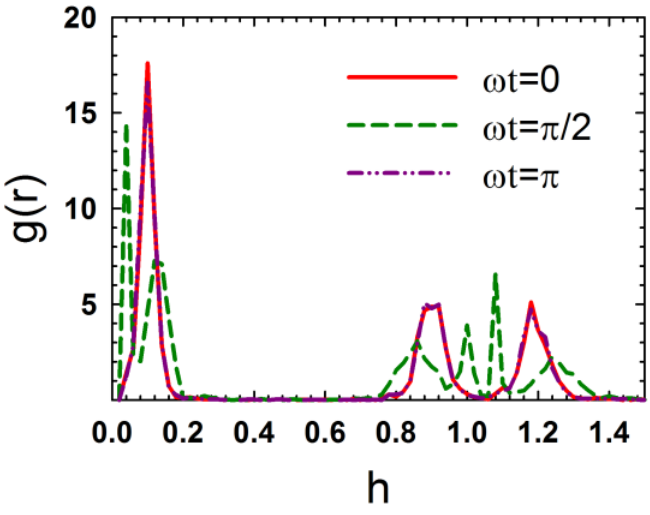

(a)

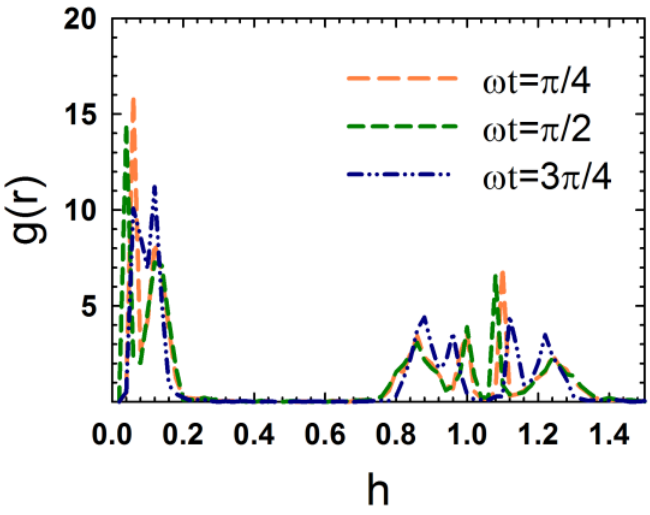

(b)

Fig. 3.19. Pair distribution function $g(r)$ at $\gamma_0 = 0.2$. (a) $g(r)$ at $\omega t = 0$, $\omega t = \pi/2$ and $\omega t = \pi$. (b) $g(r)$ at $\omega t = \pi/4$, $\omega t = \pi/2$ and $\omega t = 3\pi/4$.

It is well known that mono-disperse hard-sphere suspensions near the liquid and crystal coexistence region form an ordered crystalline structure under an oscillatory shear flow [55,56,75,76]. However, the correlation between the rheological properties and the microstructure of the suspensions has rarely been studied. Furthermore, the structure of the particles in the velocity-vorticity plane has rarely been observed due to the technical limitations. Recently, the microstructure of colloidal hard-sphere suspensions was investigated with the confocal microscopy and Brownian dynamics simulation [77]. In this study, the ordered structure of the particles in the velocity-gradient plane as well as the velocity-vorticity plane was directly observed with confocal microscopy, but the rheological properties of the suspensions were not examined. Although the correlation between rheology and microstructure is not clear yet, the shear induced ordered structure itself has been widely reported in many experimental reports for suspensions near the liquid and crystal coexistence region [55,56,75-78]. With this background, we also investigated the particles' ordering structure during the oscillatory shear flow.

To quantify the ordering of the particles, the bond order parameter [78] was adopted, which denotes the degree of local order of the particles in a single plane. The local bond order parameter ψ_6 for particle *i* is defined as follows.

$$\left|\psi_6(i)\right| = \left| \frac{1}{n_c(i)} \sum_{j=1}^{n_c(i)} e^{i6\theta(r_{ij})} \right|. \tag{26}$$

Here, $n_c(i)$ is the particle *i*'s nearest neighbor, and $\theta(r_{ij})$ is the angle between the bonded particles *i* and *j*. $\theta(r_{ij})$ is calculated by Eq. (27) in terms of the center to

center distance r_{ij} and the y component of the distance $X_{i,y} - X_{j,y}$ between the particles *i* and *j*.

$$\theta = \tan^{-1}\left(\frac{X_{i,y} - X_{j,y}}{r_{ij}} \right). \tag{27}$$

The particles were defined to be bonded when their center to center distance was within the critical distance, $r_c = 2R + 0.8\Delta x$. This corresponded to the closest distance of the particles at the flow reversal ($\omega t = \pi/2$), which was determined by the position of the first g(*r*) peak observed in the PDF (Fig. 3.19). The local bond order parameter $|\psi_6|$ includes information both on the bond and angle among the particles. In a perfectly ordered hexagonal layer, the angles $\theta(r_{ij})$ are multiples of 60°, and $|\psi_6| = 1$. For the total number of particles *N*, the local bond order parameter can be averaged as shown in Eq. (28), and it was defined as the global bond order parameter Ψ_6 within the plane.

$$\Psi_6 = \frac{1}{N}\sum_{i=1}^{N} |\psi_6(i)|. \tag{28}$$

In Fig. 3.20(a), Ψ_6 is plotted with the normalized shear stress. At low strain amplitudes where the shear stress was sinusoidal, Ψ_6 remained nearly 0 over the whole region. An increase in Ψ_6 began to appear near the flow reversal (the maximum strain) at $\gamma_0 = 0.13$, while Ψ_6 increased at an earlier time in advance to the flow reversal at higher strain amplitudes. At $\gamma_0 \geq 0.15$, an increase in Ψ_6 was clearly observed with a strong shear stress distortion. At $\gamma_0 = 0.18$, the maximum Ψ_6 and the maximum shear stress occurred at the same strain. As shown in Fig.

3.20(b), the strain at the maximum shear stress and at the maximum global bond order parameter coincided for $\gamma_0 < 0.3$. However, this relationship disappeared at $\gamma_0 = 0.35$, and this may be related with the decrease in dynamic moduli after the maximum as seen in Fig. 3.14. These results clearly demonstrate how strongly the ordered structure is related with the shear stress distortion.

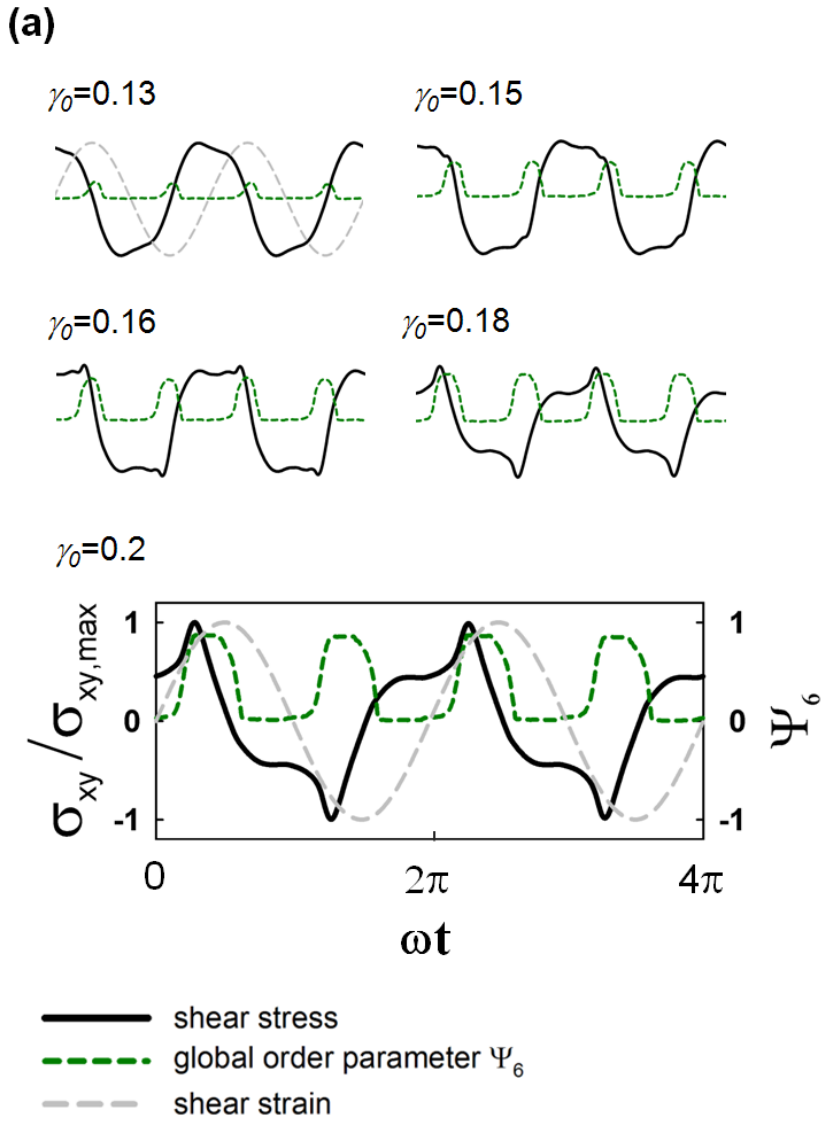

Fig. 3.20. (a) The global bond order parameter Ψ_6 and the normalized total stress.

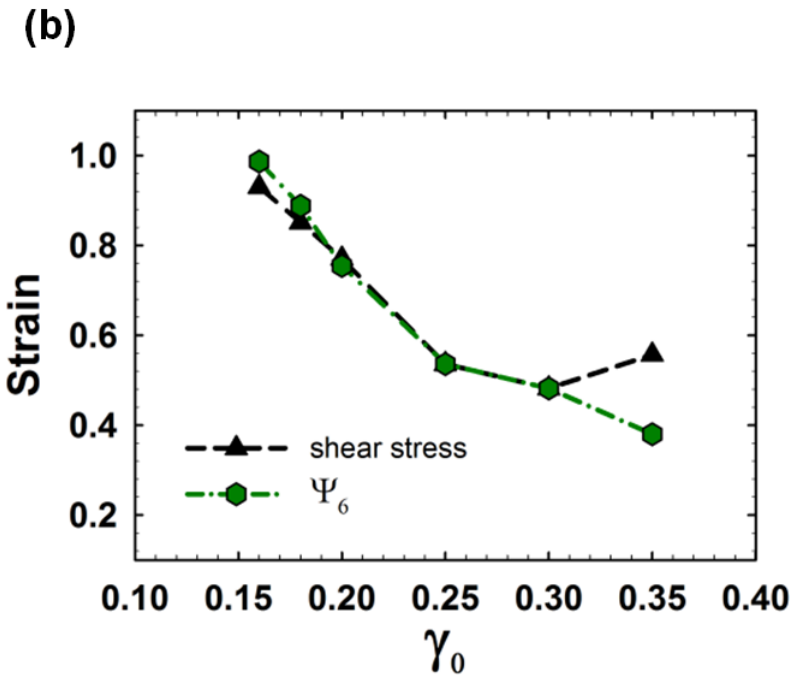

Fig. 3.20. (b) The strains at the maximum shear stress and at the maximum global bond order parameter versus strain amplitudes.

Fig. 3.21 shows the particle configuration with the local bond order parameter $|\psi_6|$ for $\gamma_0 = 0.2$, in which a distorted shear stress is clearly observed. At strain = 0 (Fig. 3.21(a) and 3.21(f)), only a few particles were aligned, and the global bond order parameter was as small as 0.03. As the strain increased, Ψ_6 increased. At $\omega t \sim 3\pi/10$, the maximum of the global bond order parameter ($\Psi_6 = 0.87$) was observed (Fig. 3.21(c)). At the flow reversal ($\omega t = \pi/2$), the ordered structure of the particles was reduced as indicated by the global order parameter of 0.76. As the strain was increased further, the structure of the suspension broke up (Fig. 3.21(d)). Ψ_6 was asymmetric before and after the flow reversal at $\omega t = \pi/4$ and $\omega t = 3\pi/4$ (Figs. 8(b) and 8(e)), and its behavior was similar to the previous results observed in the PDF (Fig. 3.19).

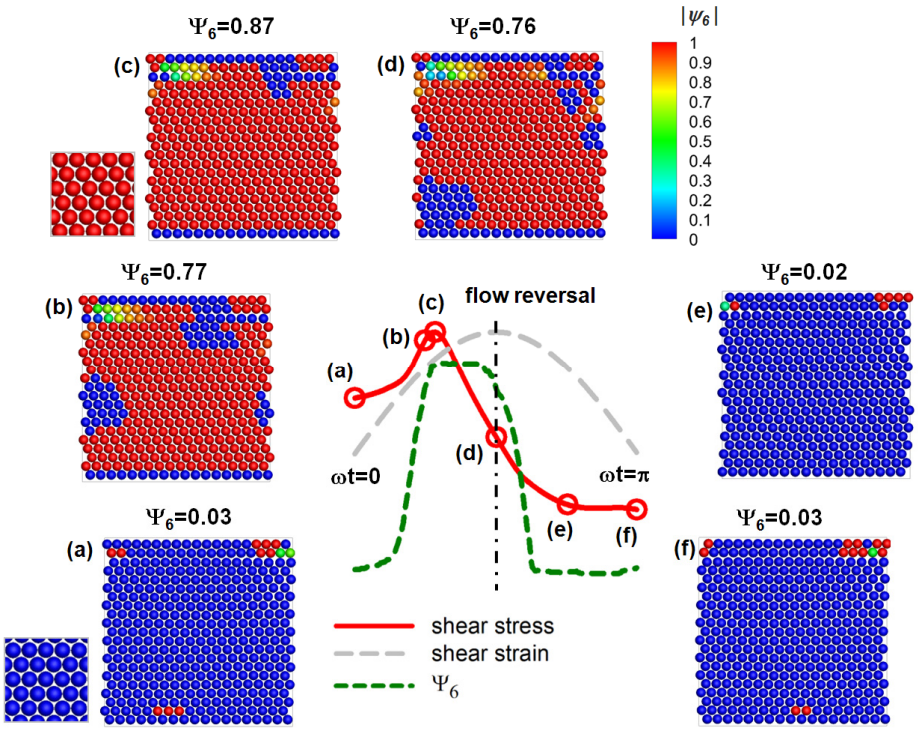

Fig. 3.21. Particle configurations with the normalized shear stress and shear strain, and the global bond order parameter at $\gamma_0 = 0.2$. (a) $\omega t = 0$, (b) $\omega t = \pi/4$, (c) $\omega t \sim 0.3\pi$, (d) $\omega t = \pi/2$, (e) $\omega t = 3\pi/4$ and (f) $\omega t = \pi$.

To further investigate the structure of the ordered particles, the bond number distribution and angular distribution were additionally analyzed. The bond between the particles was defined by two pairs of particles which have a center to center distance within a critical distance of $r_c = 2R + 0.8\,\Delta x$, and the angular distribution for the bonded particles i, j was evaluated by Eq. (27).

In Fig. 3.22(a), the bond number distribution is plotted for $\gamma_0 = 0.2$. At low strain ($\omega t = \pi/6$), most particles were not bonded, and they were dispersed without alignment. On the other hand, the number of bonded particles increased with an increase in strain ($\pi/5$ and $\pi/4$), and most particles formed two bonds (bond number = 2). As shown in Fig. 3.22(b), the bonded particles maintained bonding angles around 110º - 120º, and this signifies that the bonded particles aligned to the compressive axis. We define angles higher than 90º counterclockwise with respect to the direction of the flow to be the compressive axis direction, while those less than 90º were defined to be along the extensional direction.

A particle structure aligned to the compressive axis was also observed in experiments [77]. Using confocal microscopy, they directly observed the microstructure of mono-disperse hard-sphere suspensions in the liquid and crystal coexistence region. They focused on the change in the structure of the suspensions for varying strain amplitudes under an oscillatory shear flow, and shear induced ordering of particles in the velocity-shear gradient plane was successfully captured. In their experiments, the face-center-cubic (fcc) structure appeared at the maximum displacement (the maximum strain) while a body-centered-tetragonal (bct) structure appeared at the transient states. These structures, which were observed from the velocity-shear gradient plane (Fig. 4 in ref. [77]), matched well with our simulation results shown in Fig. 3.21 at (a) $\omega t = 0$ and (d) $\omega t = \pi/2$. In our work, the structure

of the suspensions along the vorticity direction (or 3D structures) could not be predicted because the simulation was performed in 2D space. Despite the limitation of the 2D simulation, an ordered structure in the velocity-gradient plane is similarly observed in both experiment and simulation. From this observation, we can confirm that the shear stress with strain stiffening is significantly affected by the microstructure in the velocity-gradient.

The ordered structures during strain stiffening show different characteristics compared with the structure of the hydroclusters in steady shear thickening [7,8,10,12]. Although structural alignment in the direction of the compressive axis appeared in both systems, the angular distribution of the particles was maintained in a narrower range (110º - 120º) during strain stiffening. In contrast, hydroclusters in steady shear thickening were formed with a wider range of angle distribution, around 90º - 180º [10,13,20]. In addition, the bond number was maintained at "two" in strain stiffening, which indicates that a more regularly aligned structure was formed during strain stiffening. Interestingly, the ordered structure of strain stiffening and the hydroclusters of steady shear thickening appeared at different shear rate regions. It has been reported that the hydroclusters form at high shear rates (high Peclet numbers) [10-12]. On the other hand, the ordered structure of strain stiffening was formed near the lowest shear rate region (flow reversal). These results imply that the ordered structures in steady and oscillatory shear originate from different mechanisms.

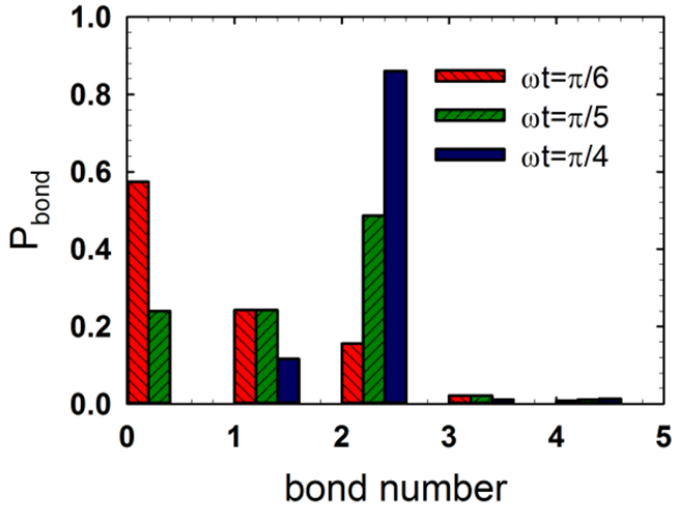

(a)

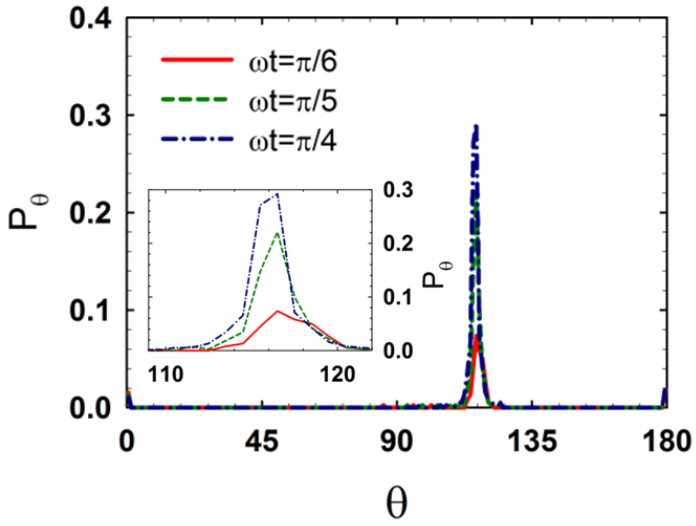

(b)

Fig. 3.22. Bond number distribution (a) and angular distribution of the particles (b) at $\omega t = \pi/6$, $\omega t = \pi/5$ and $\omega t = \pi/4$ ($\gamma_0 = 0.2$).

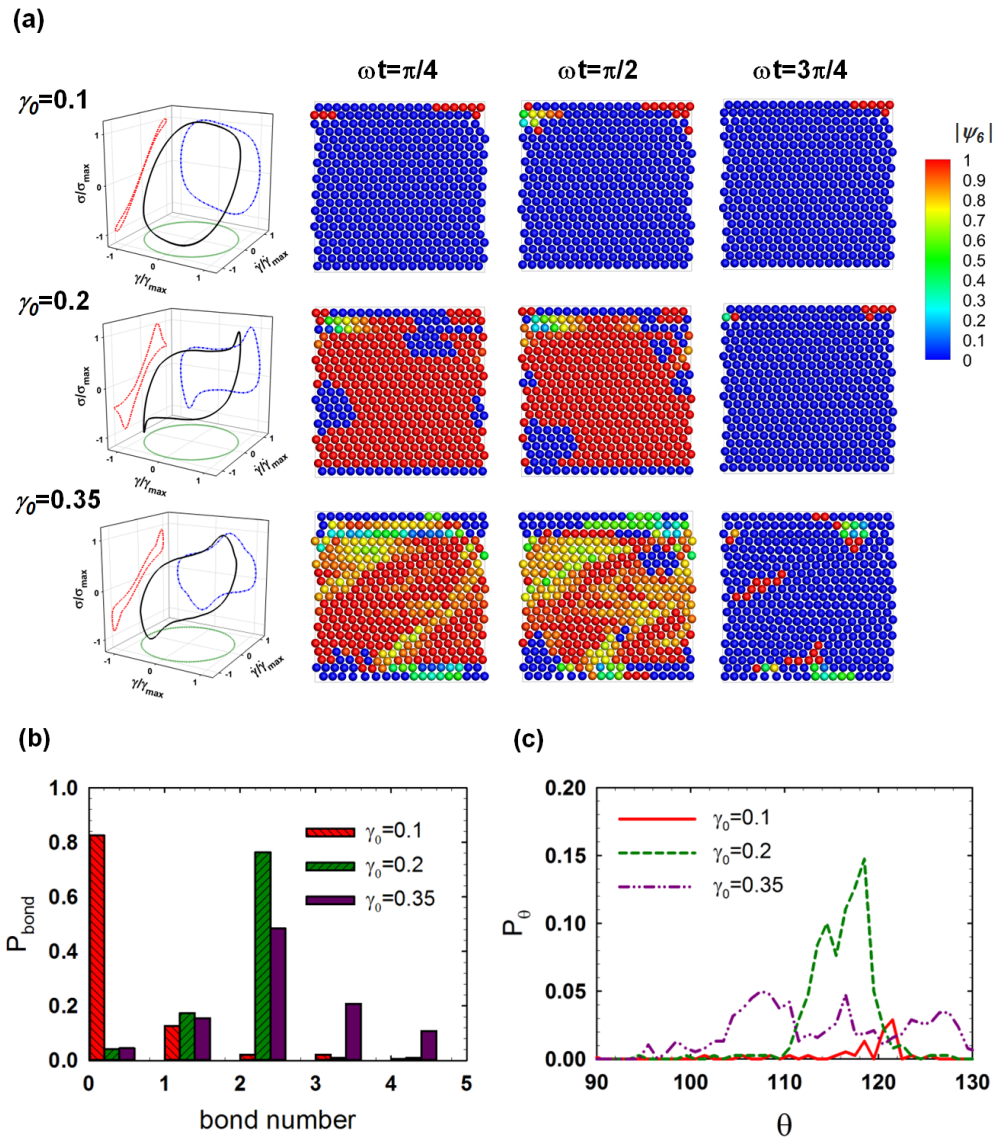

Fig. 3.23. (a) Pikpin 3D plot for shear stress, shear strain and shear rate (left). Particle configurations with the local bond order parameter at varying strain and strain amplitudes (right). (b) Bond distribution and (c) angular distribution of bonded particles at flow reversal ($\omega t = \pi/2$).

The change in the ordered structure can be correlated with the strain stiffening behavior. As seen in Fig. 3.23(a), only a few ordered structures were formed at low strain amplitudes ($\gamma_0 < 0.1$), and the sinusoidal waveform of the shear stress was well reproduced. At higher strain amplitudes, the particles became more ordered, and the distortion of the shear stress began to appear (Figs. 7 and 8). At $\gamma_0 = 0.2$, a strongly distorted shear stress was formed with a highly ordered structure, and the strain stiffening appeared there. At this region, the particles were ordered along the compressive axis with a bond number of two. At the higher strain amplitude $\gamma_0 = 0.35$, strongly disordered structures were observed in Fig. 3.23(a), and the particles with a bond number of two disappeared (Fig. 3.23(b)). With the strongly disordered structure, the angular distribution of the bonded particles appeared over a broad range (Fig. 3.23(c)). Finally, these disordered structures induced a decrease in the storage modulus.

The correlation between the degree of structural order of the suspensions and their dynamic moduli can be confirmed again by the maximum of the global bond order parameter $\Psi_{6,max}$ shown in Fig. 3.24. Interestingly, the maximum of the global bond order parameter had a similar behavior with the dynamic moduli. At the region where the dynamic moduli plateaued ($\gamma_0 = 0.01$ - 0.1), the maximum of the global bond order parameter $\Psi_{6,max}$ was below 0.05. However, beyond the critical strain amplitude $\gamma_0 = 0.13$, $\Psi_{6,max}$ suddenly increased to 0.3. The increase of $\Psi_{6,max}$ preceded the onset of strain stiffening, and this demonstrates that the ordered structure of the particles is formed in advance, and the rheological properties are affected thereafter. At $\gamma_0 = 0.2$, the structure was strongly ordered, confirmed by $\Psi_{6,max} = 0.87$, and then became less ordered when the strain amplitude was increased further ($\Psi_{6,max} = 0.81$ at $\gamma_0 = 0.35$). These results clearly

show that the structural order of the particles along the compressive axis directly affects not only the stress distortion (in Fig. 3.20) but also the dynamic moduli. Therefore, it can be concluded that the key mechanism of strain stiffening is the ordering of particles under a large strain amplitude oscillatory shear flow.

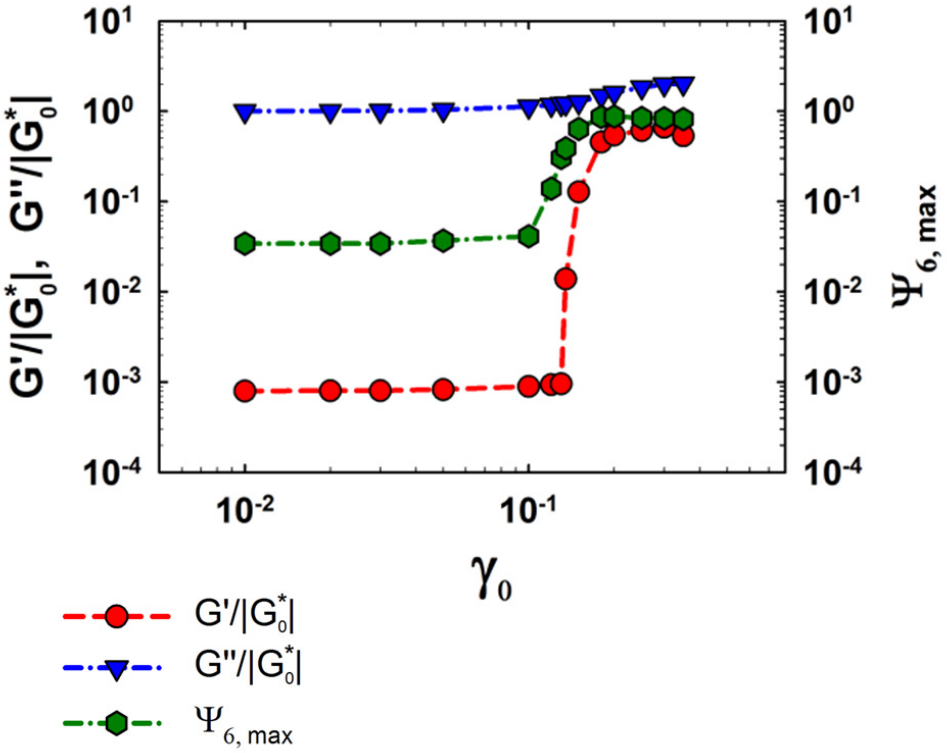

Fig. 3.24. Dynamic moduli and the maximum of the global bond order parameter $\Psi_{6,\max}$.

Chapter 4. Concluding remarks

The rheology and microstructure of a non-Brownian suspension were investigated by the lattice Boltzmann method (LBM) coupled with the smoothed profile method (SPM).

First, rheology of non-Brownian suspensions under steady shear flow was studied. The effects of the particle volume fraction and the particle Reynolds number on rheology of suspension were explored, and the correlation of local quantities such as local shear stress and local particle volume fraction were also analyzed. At low particle Reynolds number, an increase in the relative shear viscosity was observed with an increase in the particle volume fraction, and the results corresponded well with the Krieger-Dougherty relation. At high particle Reynolds number, an increase in the relative shear viscosity, which is the so-called shear thickening, was observed. To correlate the rheology and microstructure of the suspension, various structural analyses were applied. According to the pair distribution function, more particles were aligned in the compressive axis with increase of the particle Reynolds number. By analyzing the cluster size and angular distribution, we observed that larger clusters were formed at higher particle Reynolds number, and they were aligned to the compressive axis with shear thickening. The local rheology and local microstructure of the suspension were also investigated by the MOP algorithm. The time averaged local shear stress by MOP coincided well with that measured by WSS, and shear thickening at high Re_p was captured in MOP results. With an increase in the particle Reynolds number, shear thickening was enhanced with more the local shear stress fluctuations. The local stress fluctuation could be correlated with local microstructure of the suspension.

To investigate it, a linear correlation between the local particle stress and the local particle volume fraction was quantified by Pearson's correlation coefficient. When shear thickening was not strong, the Pearson's correlation coefficient maintained a value closely one, which means that they have a strong linear correlation with each other. On the other hand, a significant decrease in the Pearson's correlation coefficient was observed with shear thickening. This result means that even though the particles occupied the equivalent amount of space, they can show different rheology depending on their microstructure. It is clear that the local rheology of a suspension, which originates from a local microstructural change, affects the bulk rheology of a suspension.

Secondly, strain stiffening of non-Brownian suspensions in the liquid and crystal coexistence region was investigated. Concentrated hard-sphere suspensions in liquid and crystal coexistence region show a unique nonlinear behavior under large amplitude oscillatory shear flow, so-called strain stiffening. Even though, it has been widely observed in experiments, its key mechanism have not been explained. To clarify it, numerical simulation was performed by the lattice Boltzmann method LBM coupled with SPM. The dynamic moduli were measured for varying strain amplitudes at a fixed angular frequency. Contrary to the plateau moduli at low strain amplitudes, strain stiffening was clearly observed at high strain amplitudes. With strain stiffening, the shear stress started to show a distortion near the critical strain amplitude. This nonlinear response was quantified with Fourier transformation (FT) and stress decomposition. In the FT analysis, the relative third harmonic intensity, $I_{3/1}$ increased with the increase in the strain amplitude, and then decreased after the maximum. The slope of $I_{3/1}$ with respect to the strain amplitude was 2.0 during the increase and -1.2 for the decrease, and these values coincided

well with experiments. Using the stress decomposition, the elastic stress and viscous stress were successfully decomposed from the total shear stress. The peaks of elastic stress became stronger as the strain amplitude increased, and finally were separated into double peaks. An increment of the elastic stress was also observed near the critical strain amplitude, contrary to the decrease in the viscous stress, which means that strain stiffening was accompanied by the change in relative contribution between the elastic and viscous stresses on the total stress, or by the enhanced elasticity of the suspensions. The microstructure of the suspension was analyzed to investigate the origin of the strain stiffening. In the PDF analysis, the change in particle structure was dependent on the strain during the oscillation, and the formation of an asymmetric structure before and after the flow reversal was discovered. The distortion in the shear stress was found to be strongly correlated with the ordering of the particles during the oscillatory shear flow. Above the critical strain amplitude, an increase in Ψ_6 was clearly observed at the flow reversal (the maximum strain). In addition, the maximum of Ψ_6 and the maximum shear stress occurred at the same strain above a strain amplitude of γ_0 = 0.18. These results clearly show how strongly the ordered structure is related with the shear stress distortion. The ordered particles maintained a bond number of two with alignment to the compressive axis. The particles were distributed over a narrow range of the angular distribution (110º - 120º), which is different from the commonly reported hydroclusters in steady shear thickening. Furthermore, the ordered structure during strain stiffening was formed near the lowest shear rate region (the flow reversal), which is also remarkably different from the hydroclusters in the steady shear flow. These results imply that the ordered structures in the steady and oscillatory shear originate from different mechanisms.

The correlation between the degree of structural order of the suspensions and their dynamic moduli can be confirmed by the maximum of the global bond order parameter $\Psi_{6,\max}$. The maximum of the global bond order parameter had a similar increasing behavior with the dynamic moduli . These results clearly show that the structural order of the particles along the compressive axis directly affects not only the stress distortion but also the dynamic moduli. In conclusion, the strain stiffening of hard sphere suspensions near the liquid and crystal coexistence region was induced by the ordered structure of the particles which were aligned to the compressive axis.

Bibliography

[1] R. G. Larson, *The Structure and Rheology of Complex Fluids* (Oxford University Press, New York, 1999).

[2] H. A. Barnes, Shear-Thickening ("Dilatancy") in Suspensions of Nonaggregating Solid Particles Dispersed in Newtonian Liquids, J. Rheol. 33, 329-366 (1989).

[3] M. E. Fagan and C. F. Zukoski, The rheology of charge stabilized silica suspensions, J. Rheol. 41:373–397 (1997).

[4] B. J. Maranzano and N. J. Wagner, The effect of interparticle interactions and particle size on reverse shear thickening: hard-sphere colloidal dispersions. J. Rheol. 45:1205–1222 (2001).

[5] B. J. Maranzano and N. J. Wagner, The effect of particle size on reverse shear thickening of concentrated colloidal dispersion. J. Chem. Phys. 114:10,514–10,527 (2001).

[6] R. L. Hoffman, Explanations for the cause of shear thickening in concentrated colloidal suspensions, J. Rheol. 42, 111 (1998).

[7] P. D'Haene, J. Mewis and G. G. Fuller, Scattering dichroism measurements of flow-induced structure of a shear thickening suspension, J. Colloid Interface Sci. 156, 350–358 (1993).

[8] B. J. Maranzano and N. J. Wagner, Flow-small angle neutron scattering measurements of colloidal dispersion microstructure evolution through the shear thickening transition, J. Chem. Phys. 117, 10291 (2002).

[9] X. Cheng, J. H. McCoy, J. N. Israelachvili and I. Cohen, Imaging the microscopic structure of shear thinning and thickening colloidal suspensions, Science 333, 1276-1279 (2011).

[10] J. F Brady and G. Bossis, The rheology of concentrated suspensions of spheres in simple shear flow by numerical simulation, J. Fluid Mech. 155, 105 (1985).

[11] G. Bossis and J. F. Brady, The rheology of Brownian suspensions, J. Chem. Phys. 91, 1866 (1989).

[12] D. R. Foss, J. F. Brady, Structure, diffusion and rheology of Brownian suspensions by Stokesian Dynamics simulation, J. Fluid Mech. 407, 167 (2000).

[13] A. Sierou, J. F. Brady, Rheology and microstructure in concentrated non colloidal suspensions, J. Rheol. 46 (5), 1031-1056 (2002).

[14] W. R. Hwang, M. A. Hulsen and H. E. H. Meijer, Direct simulation of particle suspensions in sliding bi-periodic frames, J. Comput. Phys. 194(1), 742-772 (2004).

[15] S. Succi, *The Lattice-Boltzmann Equation* (Oxford University Press, Oxford, 2001).

[16] C. K. Aidun and J. R. Clausen, Lattice-Boltzmann Method for Complex Flows, Annu. Rev. Fluid Mech. 42, 439-72 (2010).

[17] A. Shakib-Manesh, P. Raiskinmäki, A. Koponen, M. Kataja and J. Timonen, Shear stress in a Couette flow of liquid-particle suspensions, J. Stat. Phys. 107, 67 (2002).

[18] P. Raiskinmäki, J. A. Åström, M. Kataja, M. Latva-Kokko, A. Koponen, A. Jäsberg, A. Shakib-Manesh and J. Timonen, Clustering and viscosity in a shear flow of a particulate suspension, Phys. Rev. E 68, 061403 (2003).

[19] J. Kromkamp, D. van den Ende, D. Kandhai, R. van der Sman and R. Boom, Lattice Boltzmann simulation of 2D and 3D non-Brownian suspensions in Couette flow, Chem. Eng. Sci. 61(2), pp.858-873 (2006).

[20] P. Kulkarni and J. Morris, Suspension properties at finite Reynolds number from simulated shear flow, Phys. Fluids 20, 040602 (2008).

[21] H. M. Laun, R. Bung and F. Schmidt, Rheology of extremely shear thickening polymer dispersions (passively viscosity switching fluids). J. Rheol. 35:999–1034 (1991).

[22] W. H. Boersma, J. Laven and H. N. Stein, Viscoelastic properties of concentrated shear-thickening dispersions. J. Colloid Interface Sci. 149:10–22 (1992).

[23] S. R. Raghavan and S. A. Khan, Shear-thickening response of fumed silica suspensions under steady and oscillatory shear, J. Colloid Interface Sci. 185, 57–67 (1997).

[24] J. Mewis and G. Biebaut, Shear thickening in steady and superposition flows effect of particle interaction forces. J. Rheol. 45:799–813 (2001).

[25] Y. S. Lee and N. J. Wagner, Dynamic properties of shear thickening colloidal suspensions, Rheol. Acta 42, 199–208 (2003).

[26] C. Fisher, C. J. G. Plummer, V. Michaud, P. E. Bourban and J. A. Månson, Pre- and post-transition behavior of shear-thickening fluids in oscillating shear, Rheol. Acta 46, 1099–1108 (2007).

[27] J. G. Nam, K. H. Ahn, S. J. Lee and K. Hyun, Strain stiffening of non-colloidal hard sphere suspensions dispersed in Newtonian fluid near liquid-and-crystal coexistence region, Rheol. Acta 50, 925–936 935 (2011).

[28] S. Jafari, R. Yamamoto and M. Rahnama, Lattice-Boltzmann method combined with smoothed-profile method for particulate suspensions, Phys. Rev. E 83, 026702 (2011).

[29] G. K. Batchelor, The stress system in a suspension of force free particles, J. Fluid Mech. 41, 545 (1970).

[30] T. Krüger, F. Varnik and D. Raabe, Particle stress in suspensions of soft objects, Phil. Trans. R. Soc. A 369, 2414-2421 (2011).

[31] Y. H. Qian, D. D'Humières and P. Lallemand, Lattice BGK models for Navier–Stokes equation, Europhys. Lett. 17. 479 (1992).

[32] A. J. C. Ladd, Numerical Simulations of Particulate Suspensions via a discretized Boltzmann Equation. Part I. Theoretical Foundation, J. Fluid Mech. 271, 285 (1994).

[33] N. Q. Nguyen and A. J. C. Ladd, Lubrication corrections for lattice-Boltzmann simulations of particle suspensions, Phys. Rev. E 66, 046708 (2002).

[34] C. K. Aidun, Y. Lu, and E. J. Ding, Direct analysis of particulate suspensions with inertia using the discrete Boltzmann equation, J. Fluid Mech. 373, 287 (1998).

[35] T. Krüger, F. Varnik and D. Raabe, Efficient and accurate simulations of deformable particles immersed in a fluid using a combined immersed boundary lattice Boltzmann finite element method, Comput Math Appl. 61, 3485-3505 (2011).

[36] Y. Sui, Y. T. Chew, P. Roy and H. T. Low, A hybrid method to study flow-induced deformation of three-dimensional capsules, J. Comput. Phys. 227 (12) 6351-6371 (2008).

[37] Y. Nakayama and R. Yamamoto, Simulation method to resolve hydrodynamic interactions in colloidal dispersions, Phys. Rev. E 71, 036707 (2005).

[38] K. Kim, Y. Nakayama and R. Yamamoto, Direct Numerical Simulations of Electrophoresis of Charged Colloids, Phys. Rev. Lett. 96, 208302 (2006).

[39] J. J. Molina, Y. Nakayama and R. Yamamoto, Hydrodynamic interactions of self-propelled swimmers, Soft Matter 9, 4923-4936 (2013).

[40] S. K. Doddi and P. Bagchi, Lateral migration of a capsule in a plane Poiseuille flow in a channel, Int. J. Multiphase Flow. 34 (10) 966-986 (2008).

[41] H. C. Andersen, D. Chandler and J. D. Weeks, Roles of repulsive and attractive forces in liquids, The equilibrium theory of classical fluids, Adv. Chem. Phys. 34, 105-155 (1976).

[42] B. D. Todd, D. J. Evans and P. J. Diavis, Pressure tensor for inhomogeneous fluids, Phys. Rev. E 52, 1627–1638 (1995).

[43] F. Varnik, J. Baschnagel and K. Binder, Molecular dynamics results on the pressure tensor of polymer films, J. Chem. Phys. 113, 4444 (2000).

[44] T. Krüger, F. Varnik and D. Raabe, Shear stress in lattice Boltzmann simulations, Phys. Rev. E 79, 046704 (2009).

[45] T. Krüger, *Computer simulation study of collective phenomena in dense suspensions of red blood cells under shear* (Springer, 2012).

[46] G. I. Taylor, The viscosity of a fluid containing small drops of another fluid, Phil. Trans. R. Soc. A 138 (834), 41-48 (1932).

[47] R. G. Cox, The motion of suspended particles almost in contact, Int J. Multiphas. Flow 1:343 (1974).

[48] I. L. Claeys and J. F. Brady, Lubrication singularities of the grand resistance tensor for two arbitrary particles, Physicochem. Hydrodyn. 11:261 (1989).

[49] E. J. Ding and C. K. Aidun, Extension of the Lattice-Boltzmann Method for Direct Simulation of Suspended Particles Near Contact, J. Stat. Phys. 112, 685-708 (2003).

[50] T. L. Dodd, D. A. Hammer, A. S. Sangani and D. L. Koch, Numerical simulations of the effect of hydrodynamic interactions on diffusivities of integral membrane protein, J. Fluid Mech. 293, 147 (1995).

[51] X. He and L. S. Luo, Lattice Boltzmann model for the incompressible Navier-Stokes equation, J. Stat. Phys. 88, 927 (1997).

[52] I. M. Krieger and T. J. Dougherty, A mechanism for non-Newtonian flow in suspension of rigid spheres, Trans. Soc. Rheol. 3, 137-52 (1959).

[53] R. J. Phillips, R. C. Armstrong, R. A. Brown, A. L. Graham and J. R. Abbott, A constitutive equation for concentrated suspensions that accounts for shear-induced particle migration, Phys. Fluids A 4, 30-40 (1992).

[54] J. L. Rodgers and W. A. Nicewander, Thirteen Ways to Look at the Correlation. Coefficient, Am. Stat. 42, 59-66 (1995).

[55] B. J. Ackerson and P. N. Pusey, Shear-induced order in suspensions of hard spheres, Phys. Rev. Lett. 61:1033–1036 (1988)

[56] B. J. Ackerson, Shear induced order and shear processing of model hard-sphere suspensions, J. Rheol. 34:553–590 (1990).

[57] K. Hyun, M. Wilhelm, C. O. Klein, K. S. Cho, J. G. Nam, K. H. Ahn, *et al.*, A review of nonlinear oscillatory shear tests: Analysis and application of large amplitude oscillatory shear (LAOS), Prog. Polym. Sci. 36, 1697–1753 (2011).

[58] M. Sugimoto, Y. Suzuki, K. Hyun, K. H. Ahn, T. Ushioda, A. Nishioka, T. Taniguchi and K. Koyama, Melt rheology of long-chain-branched polypropylenes. Rheol. Acta 46:33–44 (2006).

[59] B. Debbaut and H. Burhin, Large amplitude oscillatory shear and Fouriertransform rheology for a high-density polyethylene: experiments and numerical simulation. J. Rheol. 46:1155–76 (2002).

[60] D. Chopra, D. Vlassopoulos and S. G. Hatzikiriakos, Nonlinear rheological response of phase separating polymer blends: poly(styreneco-maleic anhydride)/poly(methyl methacrylate). J. Rheol. 44:27–45 (2000).

[61] J. G. Nam, K. Hyun, K. H. Ahn and S. J. Lee, Prediction of normal stresses under large amplitude oscillatory shear flow, J. Non-Newtonian Fluid Mech. 150:1–10 (2008).

[62] T. Lim, J. T. Uhl and R. K. Prud'homme, Rheology of self-associating concentrated Xanthan solutions. J. Rheol. 28:367–79 (1984).

[63] H. Li, H. Du, G. Chen, S. H. Yeo and N. Guo, Nonlinear viscoelastic properties of MR fluids under large-amplitude-oscillatory shear, Rheol. Acta 42:280–6 (2003).

[64] F. Gadala-Maria, A. Acrivos, Shear-induced structure in a concentrated suspension of solid spheres, J. Rheol. 24:799–814 (1980).

[65] T. Narumi, H. See, A. Suzuki and T. Hasegawa, Response of concentrated suspensions under large amplitude oscillatory shear flow, J. Rheol. 49:71–85 (2005).

[66] J. M. Bricker, J. E. Butler, Oscillatory shear of suspensions of noncolloidal particles, J. Rheol. 50:711–728 (2006).

[67] R. H. Ewoldt, A. E. Hosoi and G. H. McKinley, New measures for characterizing nonlinear viscoelasticity in large amplitude oscillatory shear, J. Rheol. 52, 1427–1458 (2008).

[68] M. Wilhelm, P. Reinheimer and M. Ortseifer, High sensitive Fourier-transform rheology, Rheol. Acta 38, 349–356 (1999).

[69] M. Wilhelm, P. Reinheimer, M. Ortseifer, T. Neidhöfer and H.-W. Spiess, The crossover between linear and non-linear mechanical behavior in polymer solutions as detected by Fourier-transform rheology, Rheol. Acta 39, 241–246 (2000).

[70] M. Wilhelm, Fourier transform rheology, Macromol. Mater. Eng. 287, 83–105 (2002).

[71] J. L. Leblanc and G. Nijman, Engineering performance and material viscoelastic analyses along a compounding line for silica-based compounds, part 2: Nonlinear viscoelastic analysis, J. APPL. POLYM. SCI. 112, 3, 1128-1141 (2009).

[72] T. Neidhöfer, M. Wilhelm and B. Debbaut, Fourier-transform rheology experiments and finite-element simulations on linear polystyrene solutions, J. Rheol. 47:1351–1371 (2003).

[73] R. Salehiyan and K. Hyun, Effect of organoclay on non-linear rheological properties of poly(lactic acid)/poly(caprolactone) blends, Korean J. Chem. Eng., 30(5), 1013-1022 (2013).

[74] K. S. Cho, K. Hyun, K. H. Ahn and S. J. Lee, A geometrical interpretation of large amplitude oscillatory shear response, J. Rheol. 49, 747–758 (2005).

[75] M. D. Haw, W. C. K. Poon and P. N. Pusey, Direct observation of oscillatory-shear-induced order in colloidal suspensions. Phys. Rev. E 57:6859–6864 (1998).

[76] J. M. McMullan and N. J. Wagner, Directed self-assembly of suspensions by large amplitude oscillatory shear flow, J. Rheol. 53, 575 (2009).

[77] T. H. Besseling, M. Hermes, A. Fortini, M. Dijkstra, A. Imhof and A. van Blaaderen, Oscillatory shear-induced 3D crystalline order in colloidal hard-sphere fluids, Soft Matter 8, 6931–6939 (2012).

[78] Y. L. Wu, D. Derks, A. van Blaaderen and A. Imhof, Melting and crystallization of colloidal hard-sphere suspensions under shear, Proc. Natl. Acad. Sci. U. S. A., 106, 10564-10569 (2009).

국문 초록

입자계 현탁액은 코팅, 프린팅 그리고 잉크젯 등과 같은 첨단 산업 공정에 널리 사용되고 있다. 공정 중에 나타나는 현탁액의 급격한 유변물성 변화는 생산 제품의 품질에 직접적인 영향을 미치게 된다. 따라서 이들의 거동을 이해하고, 컨트롤 하는 것은 매우 중요한 사안이다. 현탁액의 유변물성은, 내부에서 형성된 입자들의 미세 구조와 밀접한 연관성을 가진다고 알려져 있으며, 이 상관관계를 연구하기 위한 방법 중 하나로서 수치모사 기법이 사용이 늘어나는 추세이다. 본 연구에서는, lattice Boltzmann method (LBM) 와 smoothed profile method (SPM) 이 결합된 수치모사 기법을 이용하여, 비 브라운 입자 현탁액의 유변학적 거동을 연구하였다. 정상전단흐름 및 진동전단흐름 하 에서의 현탁액의 유변물성들을 측정하였으며, 이들을 현탁액 내의 입자 구조변화와 연관 지어 설명하고자 하였다.

먼저, 정상전단 유동 하에서의 현탁액의 상대 점도를 살펴보았다. 다양한 입자 부피 분율 및 입자 레이놀즈 수에 따른 점도 변화를 살펴보았으며, 이때, 현탁액의 국부 전단 응력 및 국부 입자 부피 분율 간 상관관계를 살펴보았다. 과거 연구들에서는, 기술적 한계에 의해 현탁액의 체적 점성만이 측정 된 바 있으나, 본 연구에서는 method of planes (MOP) 라는 기법을 도입하여 현탁액 내에서 위치에 따른 국부적 전단 응력을 측정하였다. 검증 테스트를 통해서, MOP 로부터 계산된 전단 점도 측정 결과가 벽면에서의 전단 응력으로부터 계산된 점도와 잘 일치하는 것을 확인하였다. 더불어, 본 알고리즘 적용 시 현탁액 내의 입자와 용매 각각의 스트레스가 국부적으로 나누어 계산될 수 있음을 확인하였다.

낮은 입자 레이놀즈 수 영역에서 입자 부피 분율에 따라 계산을

진행하였다. 그 결과 현탁액의 상대 전단 점도의 증가 경향이 기존에 알려진 경험식인 Krieger-Dougherty relation 와 잘 일치하는 것을 확인하였다. 고농도 영역의 경우, 입자 레이놀즈 수 증가에 따라 전단 농화 현상이 강화되기 시작하였다. 입자 구조를 분석한 결과, 전단 농화 강화에 따라 서스팬젼 내에서의 클러스터의 개수 및 크기가 증가하는 양상을 확인하였다. 클러스터들은 흐름방향에 대해 압축 방향으로 나열하고 있으며, 이러한 결과들은 선행된 연구결과와 잘 일치하였다. 전단 농화 현상과 현탁액 내의 국부 미세 구조간의 관계를 살펴보기 위해, 국부 전단 응력과 국부 입자 부피 분율 간 상간관계를 살펴보았으며, 이를 위해서 Pearson 상관관계 계수가 도입되었다. 그 결과 전단 농화 현상 심화에 따라서 국부 전단 응력과 국부 입자 부피 분율 간의 선형적 상관관계가 사라짐을 새롭게 알 수 있었다. 본 연구 결과는 현탁액 내에서 국부 미세 구조 변화가 물질 전체의 유변물성에 어떻게 반영되어 나타날 수 있는지를 잘 보여주고 있다.

다음으로, liquid and crystal coexistence 영역에 해당하는 고농도 입자 현탁액이 진동 전단 유동 하에서 나타내는 유변학적 거동에 대해 살펴보았다. Hard-sphere 현탁액은 대변형 진동 전단 유동 (LAOS) 하에서 동적 점탄성 계수가 증가하는 변형 담화 거동을 보인다고 알려져 있다. 본 현상은 정상상태 유동에서의 전단 농화 현상과는 다른 메커니즘에 의해 유발 될 것으로 가질 것으로 짐작되고 있으나, 아직까지 이에 관련해서 명확히 규명된 바는 없다. 따라서, 진동유동 하에서 나타나는 현탁액의 전단 농화 현상의 근본적인 발생 메커니즘을 설명하고자 수치해석을 진행하였다.

고정된 각진동수 하에서 변형율 진폭 증가에 따른 현탁액의 유변학적 거동을 살펴보았으며, 그 결과 임계 진폭 이상에서 변형 담화 현상이

나타나는 것을 관찰하였다. 변형 담화 현상이 나타나기 시작하는 임계 진폭 근처영역에서 비선형 전단응력이 나타나기 시작하였으며, 이는 푸리에 변환 및 응력 분해 을 통해 정량적으로 분석 되었다. 마지막으로, 전단 농화 현상의 유발 원인을 규명하기 위해, 현탁액 내 미세구조 변화를 살펴보았다. 결합 정렬 변수가 도입되었으며, 이를 통해서 현탁액 내에서의 입자들의 정렬 정도를 정량적으로 분석하였다. 그 결과, 진동 전단 흐름 하에서의 나타나는 비선형성 및 동적 탄성률의 변화가 입자들의 정렬 구조에 매우 직접적으로 영향을 받고 있다는 사실을 새롭게 확인할 수 있었다.

주요어: 유변학, 비 브라운 입자 현탁액, hard-sphere, 전단 농화, 변형 담화, lattice Boltzmann method, smoothed profile method, method of planes.

학 번: 2008-21101